UNIVERSITY OF SOUTHAMPTON

FACULTY OF ENGINEERING, SCIENCE AND MATHEMATICS

School of Engineering Sciences

Vibrational Properties of Carbon Nanotubes

by

Ignacio Rodriguez Fernandez

Thesis for the degree of Master of Philosophy

November 12, 2009

Abstract

This work investigates the limits of Continuum Theory when describing the normal modes of vibration of free single-walled carbon nanotubes (CNTs). Quantitative and qualitative differences are systematically studied between molecular dynamics (MD) simulation results and their corresponding calculations using continuum theory on a set of free CNTs. A comparison of the frequencies calculated using classical continuum theories such as Euler-Bernoulli, Timoshenko beams or Thin Shell Theory shows good agreement for long waves and progressive failure of the continuum theories as the effective wavelength becomes of the order of the interatomic distance. The physical basis of the differences in frequency between the models are brought out with novel methods. A scaling expression of the deviation is inferred from the comparative analysis. It is found that the assumption underlying in the Euler-Bernoulli model that normals to the neutral axis remain normal is the main cause for the frequency deviation. For the Timoshenko and Thin Shell models, the cause is attributed to the shape mismatch between the quantisized MD-modelled CNTs and their corresponding continuum counterparts. From the novel MD data, it has also been shown that the temperature at which the specific heat capacity changes from cubic to linear is lower than the transition temperature suggested by other authors. Finally, the wall thickness of a CNT is calculated from its fundamental MD frequency.

Acknowledgements

Thanks are due to my supervisors Dr. Hans Fangohr and Dr. Atul Bhaskar for their extensive support throughout the research; to my colleagues in the Computational Engineering and Design Group for their constant help; to the University of Southampton for the financial support of this research, letting me work on one of the most fascinating areas in science and engineering.

I would also like to give special thanks to my wife Maria and to my sons Pablo and Javier, for being so supportive during my long staying away from home.

Contents

Chapter 1

Introduction

1.1 Motivation

One of the most versatile elements, carbon is present in nature as a whole range of substances. Polymers, diamond, graphite and, most important, all life forms are based on carbon. From energy generation to plastic fabrication, industry has always taken advantage of the benefits of carbon.

New types of carbon have been discovered since 1985, when Smalley and his coworkers found a new form of carbon [1], C_{60}, which was named Buckminster Fullerene because of its resemblance to the architectural designs of Fuller [2]. It is a macromolecule of carbon atoms arranged at the vertices of hexagonal and pentagonal faces.

Carbon nanotubes were first observed in 1952 by Radushkevich and Lukyanovich [3]. In 1991, Iijima and his coworkers discovered multi-walled carbon nanotubes (MWNT) [4]. In 1993, Iijima and Bethune discovered single-walled carbon nanotubes (SWNT) [5, 6]. An individual SWNT can be visualized as a single graphite sheet rolled into a tube and capped by two hemispheric fullerenes.

Later research on the properties of CNTs has shown that carbon nanotubes (CNTs) possess unprecedented levels of strength and strain [7, 8, 9, 10, 11, 12, 13]. Since CNTs are essentially double covalent bonded macromolecules of carbon, the Young's Modulus of SWNT is around 1 TPa, whereas the modulus for steel is significantly lower (200 GPa). CNTs have also a very low density ($\sim$1.4 g/cm^3 [14]). Carbon nanotubes can easily be grouped in ropes (through Van der Waals forces), which have also high strength ($\sim$60 GPa)[15]. CNTs have an exceptional aspect ratio. Diameters on SWCNTs range from 0.6 to 1 nm, while there is no limit for their length. Nanotubes as long as 20 cm have been created [16].

Carbon nanotubes have also exceptional electrical properties. Depending on their chirality, they can behave as metals or semiconductors [17]. They are also a good candidate for room-temperature superconductors [18]. Their electrical current capacity is much higher than copper [19]. They also possess outstanding thermal properties: thermal stability up to 2800°K, significantly higher than diamond. Therefore, SWNTs are regarded as one of the most promising multifunctional materials.

The physical properties of CNTs are intimately related to their vibration characteristics. Their stiffness, which is characterised by the Young's modulus, can be estimated by measuring their thermal vibration amplitude [20, 21]. The specific heat capacity of a CNT can also be obtained from the density of the vibrational modes [22, 23]. Moreover, there is currently a debate on the vibrational origins of CNT superconductivity [24, 25, 26, 27]. It is, therefore, important to understand the modes of vibration of a carbon nanotube in great detail.

1.2 Technical Challenges

Due to their nanoscopic size, obtaining all the modes of vibration experimentally is very hard to achieve at the present time: only the three first bending modes of a CNT have been clearly observed with the aid of transmission electron microscopy and electrostatic excitations [28]. Raman spectroscopy does give limited information of some radial and in-plane vibrations [29, 30]. Also, because high energy sub-nanoscopic resolution techniques such as X-ray diffraction or electron-beam tomography may significantly alter the vibrational information of the molecule in study, modelling becomes a necessity if we are to understand the vibration modes of a CNT.

There are many ways to model the modes of a CNT, but most of them fall in one of these categories: Continuum Mechanics (CM), Molecular Dynamics (MD) and *ab initio*. On the CM side, authors treat CNTs as a beam or shell of homogeneous and isotropic material, ignoring its atomistic nature. Foe example, CNTs can be modeled as one dimensional Euler-Bernoulli beams [31, 32, 33]. More refined CM solutions, specially at high frequencies, are obtained via the Timoshenko theory [34, 35], which includes shear and rotatory inertia of the beam. A CNT can also be modelled as a thin shell hollow cylinder [36]. The classical equations are based on Love's theory of thin shells [37].

In contrast to these analytical methods from classical mechanics, so-called 'Molecular Dynamics' computer simulations can be used to simulate the motion of the atoms individually [38, 39, 40]. The results are far more accurate than those obtained with CM, although these MD methods usually require significant amounts of computational effort and cannot yet be applied to macroscopic systems [41]. Only partial results on ultrashort nanotubes have been published [42]. The most fundamental type of CNT modeling,

ab initio, relies on basic laws of physics (approximations of the Schrödinger equation) and are the most computer-intensive of all, making this method viable only when studying well-targeted modes of vibration in systems with very few atoms [43].

1.3 Research Objectives

Although studies have been performed for graphite layers and other molecular-based materials [44], a detailed description of the natural vibration frequencies of a carbon nanotube has not been found in present literature. Only partial results [45] have been published. Obtaining rough approximations of the natural frequencies of CNTs using continuum equations is still a common procedure, even at high harmonics [36, 35]. It is thus desirable to produce more precise estimations of the vibration shapes and frequencies of CNTs.

For this purpose, we investigate in this thesis the appropriateness of continuum theory when applied to carbon nanotubes. A literature review is presented in Chapter 2. Chapter 3 is an introduction to the continuum and molecular theories that we have used throughout this work; and we describe the procedure to obtain the normal modes from the continuum theories in Chapter 3. In Chapter 4 we present a novel approach: the natural frequencies and the mode shapes from simulations of CNTs. Further, the natural frequencies are calculated using continuum models and confirmed with the MD simulations. For comparing normal modes (eigenvectors) we use the mode assurance criterion (MAC), which is based on a scalar measure of the closeness of two vectors. We systematically compare the bending, twisting and stretching frequencies and study the reason for the frequency divergence amongst the models, giving a scaling explanation for the deviation. We present a novel CM-MD hybrid model, useful for investigating the cause

for the divergence of the results obtained with CM and MD methods. This method enables us to simulate large CNTs with a computational economy but marginally compromised accuracy. We also corroborate our data with a spectral analysis of a CNT in a thermal bath. We then calculate the wall thickness. The specific heat capacity of a CNT from the eigenfrequencies is calculated, and a summary of our work is given in Chapter 5, as well as proposals for future work.

Chapter 2

Literature Review

The following review summarizes findings from relevant articles in the area of carbon nanotubes, focusing on the mechanical properties of single walled carbon nanotubes (SWCNTs).

2.1 Fabrication of carbon nanotubes

Since carbon nanotubes were reported [4], many techniques have been developed in order to produce carbon nanotubes. The most common ones are arc discharge, carbon vapor deposition and laser ablation.

In the arc discharge method, first developed by Iijima [4] and later improved by Ebbensen [46], two graphite rods are connected to a power supply and placed a few millimeters apart. When the switch is turned on, a 100 A electrical current vaporizes the carbon. CNTs can be found inside the debris produced after the discharge. The electrodes of Ijima's experiment were immersed in argon at 100 Torr pressure, in contrast to the 500 Torr flow helium or argon of the Ebbbensen setup.

The chemical vapor deposition process [47] consists of placing a substrate

in an oven, heating it up to 600^oC, and slowly adding a carbon-containing gas such as methane. As the gas decomposes, it frees up carbon atoms, which recombine in the form of nanotubes, often with the aid of catalysts. According to atomic force microscope (AFM) measurements on the tip of the CNT [48], it is believed that, during CNT growth, the catalyst is located at the tip of the nanotube,

With this process, also known as catalytic chemical vapor deposition (CCVD), it is possible to produce single-walled and multi-walled carbon nanotubes. The catalyst used may vary, being iron particles [49] [50], cobalt or iron on silicon dioxe [51] [52], iron or cobalt and zeolite [49] [53] and iron on a substrate made of aluminum oxide [54].

The CCVD method is widely used today since it requires much lower temperatures for the synthesis, making cheaper the nanotube production [54]. It also allows the production of aligned SWCNTs and MWCNTs, and the control of the length, diameter and thickness of the nanotubes.

A variation of the CCVD method, introduced by Kyotani, produced aligned MWCNTs on alumina porous films using a non-catalytic chemical vapor deposition [55].

The third class of CNT production methods is laser ablation, in which the carbon is vaporized with intense laser pulses in an oven with Co and Ni as catalysts. Itproduced the largest yields (70-90 %) of nanotubes so far by tuning the boundary conditions [56]. Ultra-long (up to 4 cm) single-walled nanotubes have been produced [57] by catalytic chemical vapor deposition, and the authors suggest that it is possible to synthesize SWCNTs without any length limitation. They also show that the nanotubes grow from their tips (the catalytic Fe particles moved with the growing SWNT tips) and that whenever the CNT becomes wavy, the growth stops.

When nanotubes grow, they usually arrange in a somehow disordered fashion and are poorly stacked (30% CNT/void ratio). In order to produce CNT sheets with higher densities (95%), SWCNT have been grown by applying a strong magnetic field, normal to the deposition surface [58]. This way, CNTs grow in a straight direction and they can be thus packed more easily.

New ways of producing CNTs are being discovered continually. It has been recently claimed the fabrication of CNTs by rapidly heating grass to around 600°C. When the grass burns, and with the appropriate amount of oxygen, its vascular bundles shrink to form MWCNTs [59].

One of the biggest challenges in nanotube science is to get a detailed picture of how they form. In this direction, simulations of the carbon deposition and nanotube growth mechanisms [60] have been performed using Brenner's potential [61], which can emulate the bond formation and breaking among carbon atoms. The authors show, in a series of snapshots, how the catalyst plays an important role in the growth of nanotubes.

2.2 Mechanical properties of carbon nanotubes

CNTs behave as carbon fibres that can be stiff and flexible at the same time. They have very high Young's modulus and shear moduli, which are the most important parameters that define the mechanical stiffness of a material. The first measurement of the Young's modulus of MWNTs came from [20]. TEM was used to measure the mean-square vibration amplitudes of arc-grown MWNTs over a temperature range from room temperature to 800^oC. The average value of the Young's modulus derived from this technique for 11 tubes was 1.8 TPa; 0.40 TPa being the lowest and 4.15 TPa the highest. The authors suggest a trend for higher moduli with smaller tube diameters.

In [62] it is shown how the Young's modulus can be estimated within a lattice-dynamical model of the nanotubes, which consists of a basic cell of two carbon atoms and two basic screw operations and comparing them with other modeling methods such as molecular dynamics. The article is also one of the first to present the phonon dispersion curves of a SWCNT.

Another way to obtain the mechanical properties of a CNT is to analyze the nanotube response to an alternating applied electric potential [28]. When a static potential V_s is applied, the amplitude of the nanotube deflection is directly proportional to V_s. If the applied potential is sinusoidal, the Young modulus E_b is obtained using Euler-Bernouilli analysis of cantilever systems. As an alternative to electric fields, magnetic fields can be used [63].

Important mechanical features can also be obtained by plotting the force-deflection ratio. An atomic force microscope (AFM) has been used to check the ability of MWCNTs to bend the tubes [64]. Discontinuities in the force-deflection are explained by a buckling mechanism.

The recent development of many-body interatomic potentials by Tersoff and Brenner has enabled molecular dynamics simulations on a large number of atoms at high temperature. This provides interesting results on the mechanism of strain release under tension. This way, Nardelli et al. [65] observed spontaneous formation of double pentagon-heptagon pairs in strained nanotubes at high temperature.

2.3 Continuum models

In an attempt to exploit continuum models, which can be dealt analytically or are computationally less demanding than MD, elastic shell models have been employed [66]. Multi walled carbon nanotubes (MWCNTs) can be treated as a cylindrical shells of thickness equal to the difference of the out-

ermost and innermost radius. In addition, using classical formulae for the bending stiffness, it is noted that the actual bending stiffness is much higher than those obtained by experimental results, this is, that the continuum theory is not longer valid. The discrepancy is attributed to the atomistic hexagonal cell-type structure of CNTs. Finally, it is proposed that the effective bending stiffness of single-walled nanotubes should be regarded as an independent material parameter not related to the representative thickness by the classic bending stiffness formula.

Continuum methods have proved to be an efficient way to save computational resources. The vibration of CNTs have been used as a way to prove this [67] by showing that the vibration frequencies obtained via Timoshenko continuum theory [34], for longitudinal stretching, are very close than those obtained from fully atomistic simulations for low frequency vibrations.

Similarly, it has been shown how discrete molecular structures may be substituted by a representative volume element, in which each degree of freedom (DOF) related to bond and angle stretching is completely described by a finite element model for small deformations [68]. Authors obtain an effective thickness of the SWCNT that was slightly smaller than the inter atomic spacing between graphene sheets in graphite. The authors give, in this paper, the force constants for carbon-carbon interactions in a CNT. In order to clarify the problems risen with the Young's modulus consistency (due to the discrepancies in the effective wall thickness), the response to external hydrostatic pressure was modeled with the ring theory of continuum mechanics [69], in which the radial and axial displacements are modeled with trigonometric functions. The effective wall thickness is found to be $h = 0.617\mathring{A}$ for this model.

In [70], the authors were able to model multi-million systems by means

of the exponential Cauchy-Born rule, also known as the *method of the homogeneous deformations*, which links a flat graphene surface to a cylindrical surface through a transformation map. A relation was built between a representative cell of the lattice and an equivalent volume of the continuum, which depends only on the interatomic interactions. In [71], the same authors obtain explicit expressions for (i) the Young's modulus, (ii) Poisson's ratio, (iii) shear modulus and (iv) bending modulus and verify their validity by comparison with results from atomistic models [61], obtaining a good match for the former two but a poor match for the latter two, mainly attributed to a misbehavior in the Brenner code dealing with bond lengths.

The stiffness of a SWCNT can be estimated by measuring its vibration amplitudes at room temperature. This was done with electron micrograph images when the nanotube is clamped as a cantilever [72]. Young's modulus is obtained using a well known fourth-order wave equation.

Continuum models can be field models described by partial differential equations or their discretised counterparts, described by ordinary differential equations. In discretised continuum models, the stiffness of a CNT is fully described by its stiffness matrix, which relates applied forces to nodal displacements. In [73], and continuing the work of [74], the authors construct the stiffness matrix of a CNT by making a composite of four submatrices for a simple beam element in a space frame. Specific values for the elements in each submatrix are built by (i) assuming that the covalent bond acts as a load-bearing beam and (ii) setting up a linkage between sectional stiffness parameters and constants of molecular dynamics force fields.

Refinements in the theories lead to the *uniform Timoshenko beam theory* [34]. It improves the Euler-Bernoulli theory by incorporating cross-sectional shear and rotational inertia effects. Following the theory, the formula for lon-

gitudinal stretching, circumferential breathing, torsional twisting and lateral flexing vibration frequencies was obtained [75]. In [76], a condition necessary and sufficient for the appearance of double eigenvalues is presented.

2.4 Atomistic models of carbon nanotubes

Three main methods are commonly used to model the behavior of the atoms of a carbon nanotube: the harmonic approximation, the Brenner model and density functional theory (DFT).

Ab initio calculations are performed when it is required to obtain a detailed description of the electronic behaviour. In [77] authors use DFT to show how the electron density affects the optical spectra of SWCNTs by modeling the electron-hole interactions. In this work we will study the mechanical properties of CNTs and not the electronics, so we will focus on the harmonic approximation.

The Brenner potential [40] has its basis on the Tersoff potential for silicon [78], which is Morse-type, with some modifications: the potential does not only depend on the distance between atoms, but also on their relative positions. Brenner's achievement was to build an analogous model for hydrocarbons that also simulates the bond formation and breakage. It is short ranged so the simulations are relatively fast. The same author improved the model [61] by including better analytic functions and an extended database. It is one of the most accurate models to date and it can simulate the bond formation and breakage between carbon atoms [79], although it has two major drawbacks. First, it outputs the wrong bond lengths when the appropriate bond energy is calculated and vice versa.

The harmonic approximation method, used in computer codes such as GROMACS [39], is the fastest of all. It makes the assumption that, for low

amplitude oscillations, the atoms behave as if they oscillate over a quadratic well. In other words, only the quadratic term in the Taylor expansion of the potential that defines the covalent bond is used. This is also known as *the spring model*, and will be further explained in the next chapter.

In order to take both the advantages of continuum (fast but rough) and atomistic (more accurate but slower) simulations, a hybrid method called Multiscale Modeling [80] was developed. This method enables the simulation of a complete carbon vapor deposition chamber. The continuum model is applied where details of atomic motion were unimportant, and atomistic modeling is performed in the teeth of the CNT tip.

2.5 Polymer-Nanotube Composites

Because of their high aspect ratio and their exceptional mechanical and thermal properties, CNTs are being used as filler composites. One of the advantage of CNTs over other standard fillers is their high aspect ratio, which permits large interfacial adhesion.

The mechanical properties of polymer composites are thus enhanced by adding CNTs to the polymer. Introducing small amounts of CNTs in epoxy [81], PVA [82] [83] significantly improved the strength of the polymers. The orientation of the CNTs within the fibers can be chosen during the fabrication process by applying external magnetic fields [84]. Dispersing functionalised nanotubes over electrospun fibers of polystyrene and polyurethane increased the tensile strength [85].

The intefacial adhesion between MWCNT and the bulk polymer has been meassured [86]. It was found that nanotubes bridge voids in the film and that only a minor fraction of the CNT length was embedded within the

epoxy. With the aid of an atomic force microscope (AFM), the interfacial adhesion strength was measured, being orders of magnitude higher than standard engineering composites.

The force required to pull out a single CNT from a polymer was measured by Barber and coworkers [87] by attaching a single CNT to the tip of an AFM and inmersing the CNT into a liquid polymer. After the polymer solidifies, the nanotube is pulled away from the polymer, and the AFM records the force required for the interfacial failure. A high interfacial adhesion was measured.

All the mentioned techniques rely on the Van der Waals attraction principle for the strength reinforcement. An alternative technique consisting in the in-situ radical polymerization of nanotube composites has produced composites with covalent bonds between the polymer and the CNTs [88]. Covalent bonds were also formed by altering the nanotube surface before immersing it into the polymer [89]. The effect of inducing strong chemical bonding has also been investigated by modification of the carbon nanotube surfaces prior to individual carbon nanotube pull-out experiments [90].

2.6 Applications

Carbon nanotubes are being used for a wide range of applications. Their enormous versatility has made them being coined as 'a solution looking for a problems' [91], in clear reference to the discovery of the laser in the 60's [92].

They have extraordinary electrical conductivity, with current densities greater than 4×10^9 A/cm^2, more than 1,000 times greater than metals such as copper [93]. The most advanced electron field-emmiters are made with carbon nanotubes as their key component. This is thanks to the excellent

combination of high conductivity and the sharp tip of capped CNTs, because the electric field concentrates at the tip and this results in field emission. The low voltages required for field emission makes them the perfect candidate for microwave emission in satellites.

LED devices can also be made of CNTs [94]. Also, electrodes for batteries [95], capacitors [96], flat panel displays [97] (where each pixel is excited by one mini-electron gun) and portable x-ray devices.

Thanks to the rich chemistry of carbon, they can be functionalised in order to modify their solubility or their structure. Nano-mechanical devices such as nanobearings [98], nanooscillators [98] have also been studied.

Their pristine geometry and high conductivity make CNTs ideal for the connections in molecular electronics. They can act as switches or bistable memory units.

Nanotubes may be part of micro-scale devices, such as transistors [99] [100] [101], microscope probe tips [102] and nanomechanical resonators [103].

Due to their large surface area ($\sim$1000 m^2/g), CNTs are also used for hydrogen storage [104], protein support [105] and nano-membranes [106].

Probably the most seductive applications are being made in the field of composites, acting as a reinforcement filler. Such CNT-polymer composites are currently used for electomagnetic shielding [107]. Insulating materials such as plastic can also be turned into conductors with the addition of CNTs. Astronomical applications such as the space elevator [108] with the use of carbon nanotubes are being explored.

Chapter 3

Background and Methodology

3.1 Continuum Mechanics

The models present in this section assume their elasticity continuously distributed. Although atoms are arranged in a discrete fashion, the bulk behaviour may be adequately described by such models in the long wavelength limit. The material is treated as homogeneous, isotropic and obeying Hooke's law within the elastic limit. A piece of continuum possesses an infinite number of points, and thus an infinite number of degrees of freedom.

The full elasticity equations are too complicated to be solved, except for simple geometries, and simplifications are often made in order to obtain an approximate solution. The Euler-Bernoulli theory of beams is the simplest and most widely used for flexural motion. More complex theories include the Timoshenko beam theory and the elastic shell theory.

3.1.1 The Euler-Bernoulli Beam

In its most simple form, a CNT can be modeled as an Euler-Bernoulli (EB) beam. This approximation is good only for slender beams. It assumes that the plane cross-sections normal to the neutral axis (which coincides with the axis of the CNT) remain plane and normal during motion in addition to the usual kinematic linearity (strain-displacement) and constitutive linearity (stress-strain). The EB equation for free lateral deflection is fourth order in space and second order in time [31].

$$EIw'''' + \rho A\ddot{w} = 0, \qquad 0 \leq x \leq L \tag{3.1}$$

where L and A are the length and cross-sectional area of the beam, $w(x,t)$ is the transverse displacement of the beam from an equilibrium state, x is the position variable, t the time, ρ is the mass density per unit length, E is the Young's modulus and I is the second moment of the cross-sectional area. The prime and the dot symbols denote differentiation with respect to x and t respectively.

The Euler-Bernoulli equation of motion of a vibrating beam makes use of (a) kinematics of deformation, (b) constitutive law (material law relating stresses and strain) and (c) law of classical mechanics [109].

1. Kinematics

   The kinematics of the beam's deflections are shown in (Fig. 3.1). An undeformed beam is shown at the bottom of the figure, and the deflected beam is shown on the top. Here x is the distance from one end of the beam, u is the displacement in the axial direction x, χ the cross-section rotation, Θ the neutral axis rotation, and w the trans-

verse displacement to the neutral axis. It is usually accompanied by a rotation of the beam's cross section.

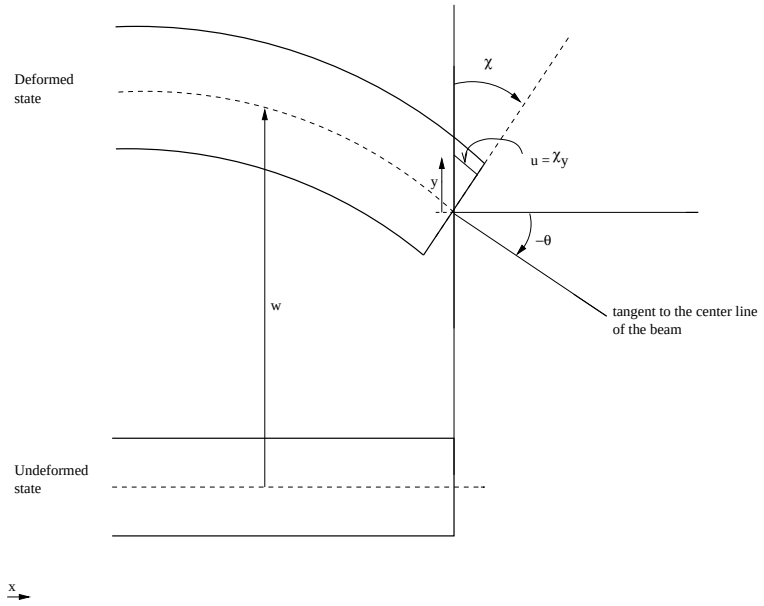

Figure 3.1: The Euler-Bernoulli beam.

The displacement in the x-direction at a cross-section at x and distance y away from the neutral axis are given by $u(x, y)$. The direct strain $\varepsilon_x(x, y)$ is given by the strain-displacement relations

$$\varepsilon_x(x, y) = \frac{\partial u}{\partial x}.$$

For the Euler beam, the assumptions were given by Kirchoff and dictate how the normals (to the beam's neutral face) behave. Kirchoff's assumptions are:

- Normals to the neutral axis remain straight (they do not bend).
- Normals remain unstretched.

- Normals remain normal.

With the normals straight and unstretched, we can assume that there is negligible strain in the y direction. Because normals remain normal to the neutral axis, the x and y dependence in $u(x, y)$ becomes explicit

$$u(x, y) = \chi(x)y.$$

With explicit x dependence in u, the direct strain throughout the beam is given by

$$\varepsilon_x(x, y) = \frac{\partial \chi(x)}{\partial x} y.$$

Finally, with normals always normal, we can tie the cross section rotation to the neutral axis rotation, and eventually to the beam's displacement w,

$$\chi(x) = -\Theta(x) = -\frac{\partial w}{\partial x},$$

which is the slope of the central line of the beam.

2. Constitutive Law

The constitutive equation relates the stresses and the strains in an elastic medium. The generalised Hooke's law relates the six stress components and the six strain components via two independent elastic constants for isotropic materials. Because there is only one non-zero stress component σ_x for beam bending, the constitutive for this one-dimensional case simplifies to

$$\sigma_x(x, y) = E\varepsilon_x(x, y) \tag{3.2}$$

where E is the modulus of elasticity. Note that the stress and strain are functions of the entire beam cross section (i.e. they can vary with y).

3. Resultants

If we were to cut a beam at a point x, we would find a distribution of direct stresses $\sigma_x(y)$ and shear stresses $\sigma_{xy}(y)$,

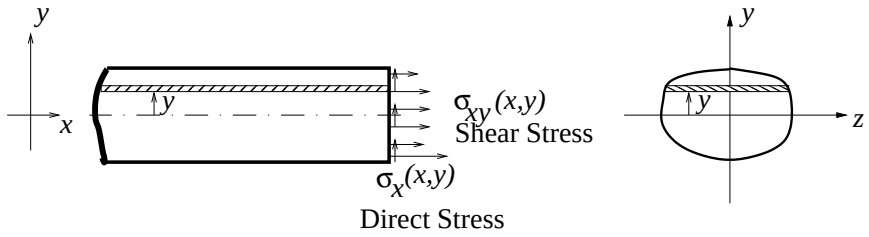

Figure 3.2: Shear Stress.

Each small portion of direct stress acting on the cross section creates a moment about the neutral axis ($y = 0$). The moment stress resultant M is the moment of distribution of the stress σ_x acting on the cut-face of the beam, integrated over the cross-sectional area,

$$M(x) = \iint y\sigma_{xy}(x, y)\,\mathrm{d}y\,\mathrm{d}z. \tag{3.3}$$

where z is the coordinate pointing in the direction of the beam width (out of the plane of the paper). The integration is over the cross-sectional area. Similarly, the shear stresses on the cross-section gives the shear resultant $V(x)$,

$$V(x) = \iint \sigma_{xy}(x, y)\,\mathrm{d}y\,\mathrm{d}z. \tag{3.4}$$

There is one more force resultant that we can define for completeness.

The sum of all direct stresses acting on the cross-section is known as N,

$$N(x) = \iint \sigma_{xy}(x, y)\, \mathrm{d}y\, \mathrm{d}z. \tag{3.5}$$

$N(x)$ is the direct force integrated over the cross-section of the beam at a cross-section at x, yet it does not play a role in beam theory since it does not cause a displacement w and the contribution to the total strain energy are often insignificant. However, it plays a role in the axial vibration of rods.

4. Force equilibrium

Consider a slice of the beam of length $\mathrm{d}x$ in the x direction as shown in figure 3.3. The equilibrium equations describe how the beam carries external transverse loads with its internal stresses. Rather than deal with these stresses themselves, we choose to work with the resultants since they are functions of x only (and not of y).

To enforce equilibrium, consider the balance of forces and moments acting on a small section of beam.

Equilibrium in the y-direction gives the equation for the shear resultant V,

$$\frac{\mathrm{d}V}{\mathrm{d}x} = -p \tag{3.6}$$

Moment equilibrium about a point on the right side of the beam gives the equation for the moment resultant M,

$$\frac{\mathrm{d}M}{\mathrm{d}x} = V \tag{3.7}$$

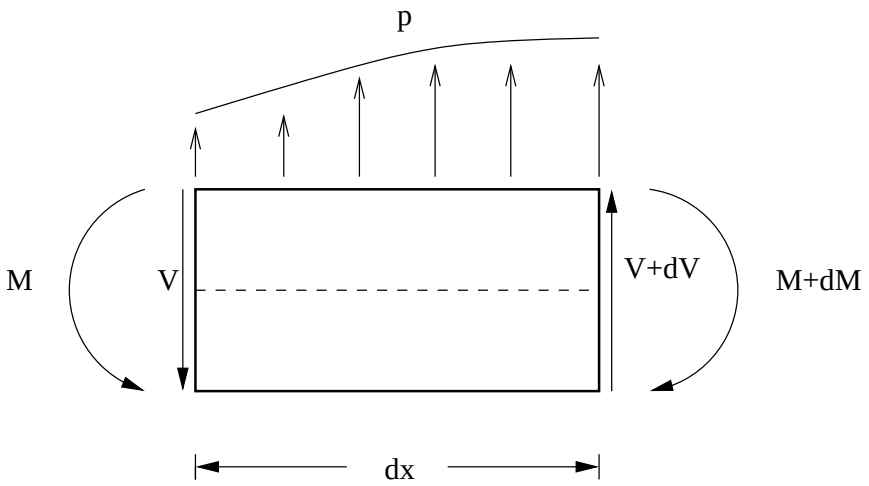

Figure 3.3: Force equilibrium.

and thus

$$\frac{d^2M}{dx^2} = -F \tag{3.8}$$

where F is the external force applied per unit length. Substituting the expression obtained for M we get the Euler-Bernoulli equation

$$\frac{d^2}{dx^2}\left(EI\frac{d^2w}{dx^2}\right) = F. \tag{3.9}$$

Under harmonic motion, the external pressure load is equal to the inertia force,

$$F_{inertia} = m\frac{d(velocity)}{dt} = m\ddot{w} = \rho A\ddot{w} \tag{3.10}$$

The double dot $\ddot{(\,)}$ symbol denotes differentiation with respect time, and m is the mass per unit length of the beam.

$$m = \rho A \tag{3.11}$$

where A is the beam's cross-section area and ρ is the density of the material.

The Euler-Bernoulli equation for lateral deflection thus becomes [31]

$$EIw'''' + \rho A\ddot{w} = 0, \qquad 0 \leq x \leq L \tag{3.12}$$

where L is the length of the beam, $w(x,t)$ is the transverse displacement of the beam from an equilibrium state, x is the position variable, t is time, E is the Young's modulus and I is the second moment of the cross-sectional area. The $(\ )'$ and $\ddot{(\ )}$ symbols denote differentiation with respect to x and t respectively.

3.1.2 Torsional Vibrations

The torsional and the extensional motion are governed by the second order wave equation -both in time and space [110]

$$u'' \ + (1/a^2)\ddot{u} = 0 \tag{3.13}$$

where u is the angular rotation and $a = (G/\rho)^{1/2}$ is the torsional wave speed. Extensional motion is described by a partial differential equation (PDE) of the same form as equation 3.13 where u is the longitudinal displacement of a point on the cross section at x and $a = (E/\rho)^{1/2}$ is the extensional wave speed.

3.1.3 Timoshenko beam bending model

Timoshenko's theory of beam bending constitutes an improvement over the Euler-Bernoulli theory as it incorporates shear effects. Timoshenko's equations of motion are [34]

$$\kappa GA(\psi + w')' = \rho A\ddot{w}, \qquad 0 \leq x \leq L \tag{3.14}$$

$$\kappa GA(\psi + w') - EI\psi'' = \rho I\ddot{\psi}, \quad 0 \leq x \leq L \tag{3.15}$$

where $w(x,t)$ represents the transverse displacement of the beam and the new variable $\psi(x,t)$ is the rotation of the cross-section of the beam with respect to the vertical direction. Here, the quantities A, ρ, E and I are the same as for the Euler-Bernoulli equation. G is the shear modulus and κ is the Timoshenko shape factor, a constant that depends only on the geometry of the cross-section of the beam.

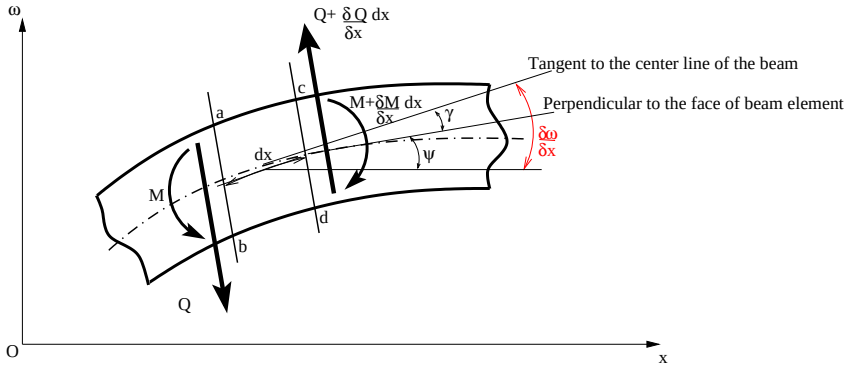

Figure 3.4: The Timoshenko beam element.

Let's consider the prismatic bar delimited by the points a,b,c and d. M is the bending moment and Q is the shearing force. The configuration of the beam is then determined by the displacement w of its center of gravity and the rotation ψ. The angle of shear is denoted by γ and it is the difference between the angle of the tangent to the beam's midline $\partial\omega/\partial x$ and the perpendicular to the right face of the beam element. Thus, for small deflections of the beam, the following kinematic relationship represents the approximation inherent in Timoshenko's theory

$$\frac{\partial w}{\partial x} = \psi + \gamma. \tag{3.16}$$

The bending moment is given by

$$M = -EI\frac{\partial \psi}{\partial x} \tag{3.17}$$

and the shearing force by

$$Q = kGA\left(\frac{\partial w}{\partial x} + \psi\right). \tag{3.18}$$

The equations of motion for rotation and translation are now coupled and we have a pair of simultaneous PDEs in two field variables $w(x,t)$ and $\psi(x,t)$

$$kGA\left(\frac{\partial w}{\partial x} + \psi\right) - EI\frac{\partial^2 \psi}{\partial x^2} = -\rho I\frac{\partial^2 \psi}{\partial t^2}, \qquad 0 \leq x \leq L \tag{3.19}$$

$$kGA\left(\frac{\partial^2 w}{\partial x^2} + \frac{\partial \psi}{\partial x}\right) = \rho A\frac{\partial^2 w}{\partial t^2}, \qquad 0 \leq x \leq L. \tag{3.20}$$

As before, $w(x,t)$ represents the transverse displacement of the beam and the new dependent variable $\psi(x,t)$ is the angle of deflection of the cross-section of the beam with respect to the vertical direction.

3.1.4 Thin Shell Theory

It is also possible to model a CNT using Thin Shell Theory. We will limit our study to the well-established Love's equations [37], which assumes the following: (i) the thickness of a shell is small compared to the characteristic dimensions on the directions normal to the thickness, (ii) the deflections of the shell are small and (iii) normals to the mid surface of the shell remain normal and the shell thickness remains unchanged. The corrections made by Donell-Mushtari [111, 112] can be then applied, in which only the oscillations

normal to the mid surface of the shell are studied. Stretching and twisting modes are thus excluded in our shell model of the CNTs.

Consider the equilibrium of all forces along the x-axis according to Fig. 3.5. This leads to [113]

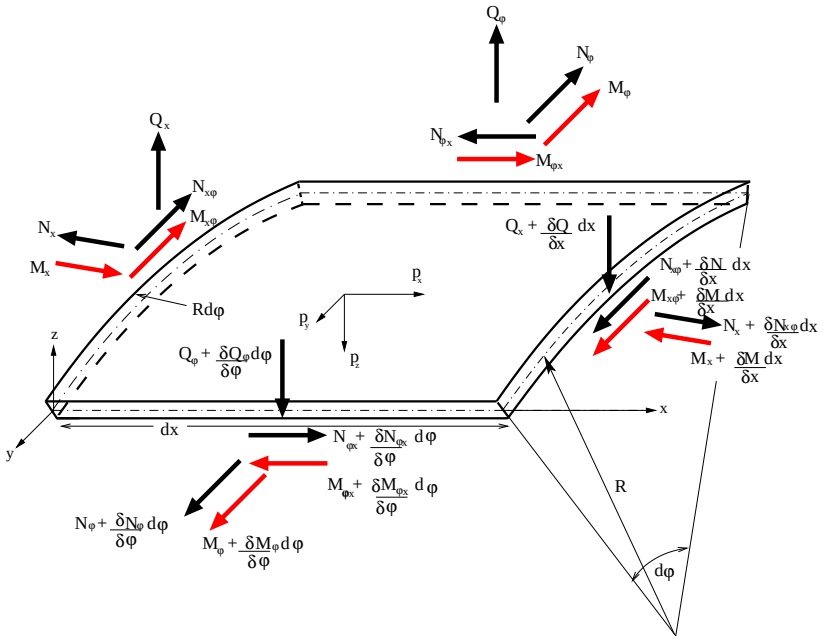

Figure 3.5: Unit forces and moments acting upon the thin shell element.

$$\left(N_x + \frac{\partial N_x}{\partial x}dx\right) Rd\varphi - N_x Rd\varphi + \left(N_{\varphi x} + \frac{\partial N_{\varphi x}}{\partial \varphi}d\varphi\right) dx - N_{\varphi x}dx + p_x Rd\varphi dx = 0. \tag{3.21}$$

Re-arranging of the previous equation, and doing the same for the moments, we get the following relationships:

1. For force equilibrium in the x, y and z directions:

$$R\frac{\partial N_x}{\partial x} + \frac{\partial N_{\varphi x}}{\partial \varphi} + Rp_x = 0 \tag{3.22}$$

$$\frac{\partial N_\varphi}{\partial \varphi} + R\frac{\partial N_{x\varphi}}{\partial x} - Q_\varphi + Rp_y = 0 \tag{3.23}$$

$$R\frac{\delta Q_x}{\partial x} + \frac{\partial Q_\varphi}{\partial \varphi} + N_\varphi + Rp_x = 0 \tag{3.24}$$

If there are no external forces upon the shell, the inertial forces under harmonic oscillations are given by

$$p_x = -\rho h\frac{\partial^2 u}{\partial t^2} \tag{3.25}$$

$$p_y = -\rho h\frac{\partial^2 v}{\partial t^2} \tag{3.26}$$

$$p_z = -\rho h\frac{\partial^2 w}{\partial t^2}. \tag{3.27}$$

Here $u(\varphi, x)$, $v(\varphi, x)$ and $w(\varphi, x)$ are the axial, tangential and radial deformations of the shell

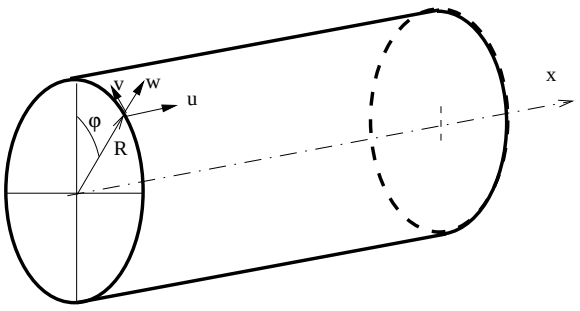

Figure 3.6: The three types of elementary displacements on a cylindrical shell.

Note that the variable w used in thin shell theory for radial displacements does not correspond to the vertical displacement in beam theories, also denoted by w.

2. Moment equilibrium around the x, y and z axis, after neglecting the terms containing the second power of the elementary length dx:

$$R\frac{\partial M_x}{\partial x} + \frac{\partial M_{\varphi x}}{\partial \varphi} - RQ_x = 0 \tag{3.28}$$

$$R\frac{\partial M_{x\varphi}}{\partial x} + \frac{\partial M_{\varphi}}{\partial \varphi} + RQ_{\varphi} = 0 \tag{3.29}$$

$$N_{\varphi x} = N_{x\varphi} \tag{3.30}$$

For cylindrical shells, the force and moment stress resultants are

$$N_x = \int_{-h/2}^{h/2} \sigma_x \left(1 - \frac{z}{R}\right) dz, \qquad N_y = \int_{-h/2}^{h/2} \sigma_y dz \tag{3.31}$$

$$N_{x\varphi} = N_{\varphi x} = \int_{-h/2}^{h/2} \tau_{xy} \left(1 - \frac{z}{R}\right) dz \tag{3.32}$$

$$M_x = \int_{-h/2}^{h/2} \sigma_x \left(1 - \frac{z}{R}\right) z dz, \qquad M_y = \int_{-h/2}^{h/2} \sigma_y z dz \tag{3.33}$$

$$M_{xy} = -\int_{-h/2}^{h/2} \tau_{xy} \left(1 - \frac{z}{R}\right) z dz, \qquad M_{yx} = \int_{-h/2}^{h/2} \tau_{yx} z dz. \tag{3.34}$$

They are forces and moments of the stress distribution over the thickness for unit length along the edge of the shell. There are several theories for thin shell deformations. Each differ on how and when the terms z/R and

h/R are to be neglected. The stress-strain relationship (constitutive law), for plane stress, is given by

$$\sigma_x = \frac{E}{1-\nu^2}(\varepsilon_x + \nu\varepsilon_y) \tag{3.35}$$

$$\sigma_y = \frac{E}{1-\nu^2}(\varepsilon_y + \nu\varepsilon_x) \tag{3.36}$$

$$\tau_{xy} = G\gamma_{xy}. \tag{3.37}$$

When corrections are made by Donell-Mushtari [111] [112], the tangential displacements u and v and their derivatives are neglected in expressing ε_x and ε_y

$$\varepsilon_x = \varepsilon_1 - z\chi_1, \qquad \varepsilon_y = \varepsilon_2 - z\chi_2 \tag{3.38}$$

$$\gamma_{xy} = \gamma_{12} - 2z\gamma_{12} \tag{3.39}$$

$$\varepsilon_1 = \frac{\partial u}{\partial x}, \qquad \varepsilon_2 = \frac{\partial v}{R\partial\varphi} - \frac{w}{R}, \qquad \gamma_{12} = \frac{\partial u}{R\partial\varphi} - \frac{\partial v}{\partial x} \tag{3.40}$$

Stretching and twisting modes are thus excluded in this shell model of the SWCNTs. The reason for choosing the Donnell-Mushtari approximation are their accurate natural frequency predictions when compared with experimental results [114] [115].

3.2 Molecular Dynamics

In contrast to the modelling of CNTs as continuous objects as in section 3.1, we now describe discrete modelling approaches that consider each atom

individually. A carbon nanotube can be regarded as a large molecule consisting of carbon atoms. The atomic nuclei can be approximated by pointlike masses. The general expression of the total potential energy, omitting the electrostatic and non bonded interactions, is a sum of energies

$$U = \frac{1}{2}\sum_i \sum_{j\in N_1(i)} U_r(i,j) + \frac{1}{3}\sum_i \sum_{(j,k)\in N_2(i)} U_\theta(i,j,k) + \frac{1}{4}\sum_i \sum_{(j,k,l)\in N_3(i)} U_\phi(i,j,k,l) \tag{3.41}$$

where $N_1(i)$ is the set of nearest neighbour indices of atom i, $N_2(i)$ is the set of pairs of nearest neighbour indices of atom i relevant for bond angle bending and $N_3(i)$ is the set of triplets of indices of neighbour of atom i that have to be considered for dihedral angle torsion nearest neighbour indices of atom i. $U_r(i,j)$ is the potential energy associated with bond stretching, $U_\theta(i,j,k)$ that for bond angle bending, and $U_\phi(i,j,k,l)$ for dihedral angle torsion. For low amplitude deviations of the atoms from their equilibrium positions, the potential functions can be approximated by quadratic forms

$$U_r = \frac{1}{2}k_r(\Delta r)^2, U_\theta = \frac{1}{2}k_\theta(\Delta\theta)^2, U_\phi = \frac{1}{2}k_\phi(\Delta\phi)^2 \tag{3.42}$$

where Δr, $\Delta\theta$ and $\Delta\phi$ respectively are the deviations from the interatom distance, interbond angle and out-of-plane angle at rest. k_r is the bond stretching force constant, k_θ is the bond twisting angle stretching force constant and k_ϕ is the bond twisting stiffness, respectively. These empirical constants were taken from literature [116] [117] and converted to S.I. units: $k_r = 196316.45\text{KJ}\cdot\text{mol}^{-1}\cdot\text{nm}^{-2}$, $k_\theta = 263.70866\text{KJ}\cdot\text{mol}^{-1}\cdot\text{rad}^{-2}$, $k_\phi = 83.717036\text{KJ}\cdot\text{mol}^{-1}\cdot\text{rad}^{-2}$. When weak forces (e.g. Van der Waals) were included in the model, the effect on the normal mode frequencies was not significant. Simulations were run with the CNT placed free in vacuum.

3.3 Normal Mode Analysis using Continuum Mechanics

3.3.1 Euler-Bernoulli Frequency Equation

A general solution to the Euler-Bernoulli equation can be shown to be

$$w = \widehat{A}\cosh\beta x + \widehat{B}\sinh\beta x + \widehat{C}\cos\beta x + \widehat{D}\sin\beta x \tag{3.43}$$

The boundary conditions for a free-free beam (i.e. free at both ends) of length L are

at $x = 0$, $x = L$:
$M = 0$ (or $\frac{d^2w}{dx^2} = 0$) and $V = 0$ (or $\frac{d^3w}{dx^3} = 0$)

which finally leads to the frequency equation

$$\cosh(\beta L)\cos(\beta L) - 1 = 0 \tag{3.44}$$

where $\beta^4 = \frac{\rho A}{EI}\omega^2$, ω the angular frequency, $\omega = 2\pi f$ and f the frequency of the natural mode of vibration. We solved this frequency, in its non dimensionalised form, using the bisection method.

The solutions appear in the ratio 1:2.756:5.403:8.933:13.342:18.636, etc. when we normalize to the first fundamental frequency. Note that these ratios are independent of the material and dimensions of the beam.

3.3.2 Torsional and stretching natural frequencies

For torsional and stretching modes of a free beam, the solution to equation (3.13) give rise to the following allowed frequencies:

$$\omega_T^i = (i\pi/L)(G/\rho)^{1/2}, \qquad \omega_S^i = (i\pi/L)(Y/\rho)^{1/2} \tag{3.45}$$

with i = 1,2,3..., where the subscripts refer to torsion and stretching respectively. When normalised against the first torsional and stretching frequencies respectively, the ratios appear as the natural numbers $\omega_T^i/\omega_T^1 = i, \qquad \omega_S^i/\omega_S^1 = i$

3.3.3 Non-dimensionalisation of Timoshenko natural frequencies

We use the Levinson and Cooke [118] frequency formula for Timoshenko beams. After non-dimensionalisation [119] of length and time, and being M the mass of the CNT per unit of length, $\hat{x} = x/L, \quad \hat{z} = z/L, \quad \hat{t} = t\left(\frac{ML^4}{EI}\right)^{-1/2}, \quad \hat{w} = w\left(\frac{ML^4}{EI}\right)^{-1/2}$, the frequencies will be given by the roots ω_i of the following equation

$$2 + \frac{\hat{\lambda}_1\hat{\alpha}_1}{\hat{\lambda}_2\hat{\alpha}_2} - \frac{\hat{\lambda}_2\hat{\alpha}_2}{\hat{\lambda}_1\hat{\alpha}_1}\text{sinh}\hat{\lambda}_1\text{sinh}\hat{\lambda}_2 - 2\text{cosh}\hat{\lambda}_1\text{cosh}\hat{\lambda}_2 = 0 \tag{3.46}$$

where

$$\hat{\alpha}_{1,2} = \pi_1\pi_2 \cdot \hat{\omega}^2 \pm \hat{\lambda}_{1,2}^2$$

$$\begin{aligned} \hat{\lambda}_{1,2}{}^2 \;=\; & \Big[(\frac{1}{2}\pi_1(1+\pi_2)\hat{\omega}^2)^2 + (1-\pi_1{}^2\pi_2\hat{\omega}^2)\hat{\omega}^2\Big]^{\frac{1}{2}} \pm \\ & \pm \frac{1}{2}\pi_1(1+\pi_2)\hat{\omega}^2 \end{aligned} \tag{3.47}$$

and the two nondimensional π-groups are $\pi_1 = R^2/L^2, \qquad \pi_2 = \frac{E}{\kappa G}$, where R is the radius the beam were it circular and κ is the Timoshenko shear coefficient. In theory, the roots ω_i will depend on two nondimensional

parameters, π_1 and π_2, in the Timoshenko frequency problem. In practice, however, we will use as a variable only one of them, π_1, since π_2 depends on material properties that do not dramatically change from one beam to another. We choose $\pi_2 = 4.0$ for our calculations, a typical value in beam mechanics.

The Timoshenko frequencies depend on the slenderness of the beam, as it is shown in Fig. 3.7. The code for finding the frequency roots can be found in Appendix **??**. As a check, note in Fig. 3.7 that the Timoshenko normalised frequencies converge to the Euler-Bernoulli ratios (seen in subsection 3.3.1) as $r_g/L \to 0$.

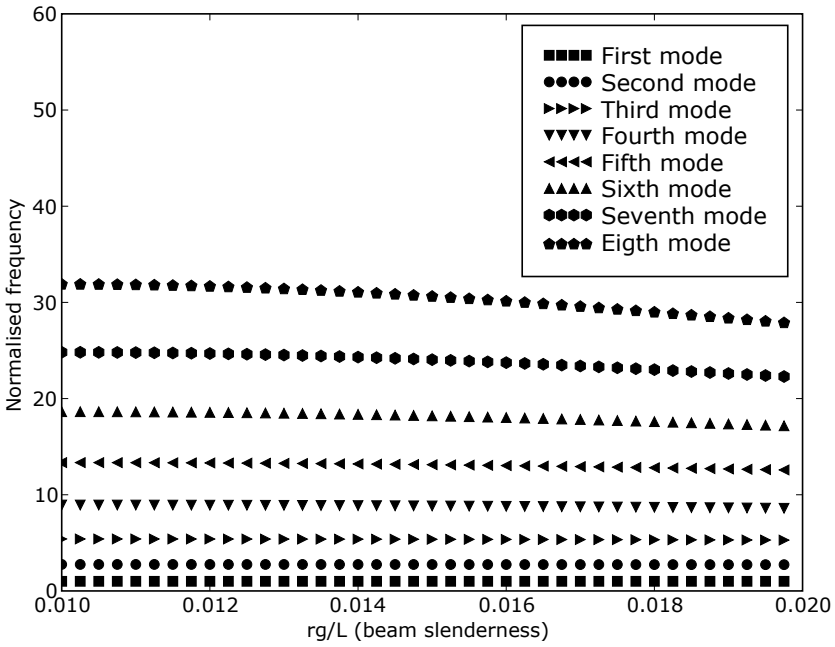

Figure 3.7: Timoshenko frequencies versus beam slenderness

3.3.4 Thin shell hollow cylinder natural frequencies

Finally, for the Thin Shell case, the frequency formula for the radial vibrations is given by Soedel [114]

$$\omega_{mn}^2 = \frac{\frac{Eh\eta_m^4}{R^2L^4\left(\frac{n^2}{R^2}+\frac{\eta_m^2}{L^2}\right)^2} + D\left(\frac{n^2}{R^2}+\frac{\eta_m^2}{L^2}\right)^2}{\rho h} \tag{3.48}$$

where n and m denote the number of radial and longitudinal antinodes of the standing wave, h is the nanotube shell thickness, $D = \frac{Eh^3}{12(1-\mu^2)}$ is the bending stiffness and η_m are the roots of the analogous free-free beam equation

$$\eta_1 = 4.730 \quad \eta_2 = 7.853 \quad \eta_3 = 10.996 \quad \eta_4 = 14.137$$

and for large m: $\eta_m = (2m+1)\,\pi/2$

The constants we have used are: $E = 1.0 \times 10^9 \mathrm{N/mm^2}$ (Young's Modulus), $\mu = 0.33$ (Poisson's ratio), $\rho = 2.21 \times 10^{-6} \mathrm{Ns^2/mm^4}$ (mass density), $h = 3.0 \times 10^{-12} \mathrm{mm}$ (shell thickness). Since it is essentially impossible to measure the actual width of an atom, the shell thickness h becomes an adjustable parameter that takes unrealistic small values once (i) the high value of the Young's modulus of a CNT is introduced in the formula (3.48) and (ii) low frequencies are fitted to the E-B model for long beams.

The thin shell problem generates a set of frequency points depending on the radial and longitudinal mode numbers n and m. As a check, we calculated the frequencies for the original setup from [114] and they are shown in Fig. 3.8. It can be seen that the lowest frequency must not correspond to the first bending mode [113].

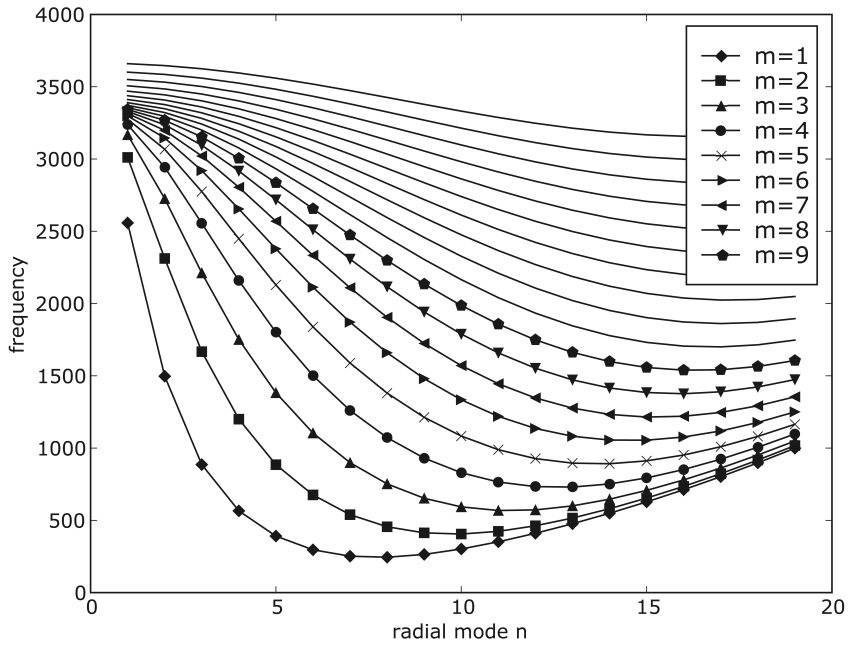

Figure 3.8: Non-normalised Thin Shell frequencies, following [114]. Diamonds represent the first mode, squares the second, and so on.

Chapter 4

Normal Mode Analysis using Molecular Dynamics

4.1 Methodology

Normal modes of vibration are simple harmonic oscillations about a local potential energy minimum. Any motion can be expressed as a sum of normal modes for a harmonic potential. Near the minimum, the potential can be approximated by a harmonic potential, and any small amplitude motion can still be well approximated by a superposition of normal modes.

Each mode is defined by an eigenvector and its corresponding eigenfrequency, ω. The eigenvector (or mode shape) contains the amplitude and direction of motion for each atom. All atoms oscillate at the same eigenfrequency, ω_i.

The energy terms in equation (3.41) are quadratic forms in terms of $3N$ generalised co-ordinates of the problem (3 positional co-ordinates for each atom). If q_i is the ith generalised co-ordinate, then the harmonic approximation of the potential energy is given by

$$U = (1/2)\mathbf{q}^T\mathbf{H}\mathbf{q}, \tag{4.1}$$

where $\mathbf{q}(t)$ is the vector of generalised co-ordinates $\{q_1(t), q_2(t), ..., q_{3N}(t)\}$ as a function of time t and $\mathbf{H}$ is the Hessian (also known as the stiffness matrix in theoretical mechanics literature) of the potential energy:

$$\mathbf{H} = \begin{pmatrix} \frac{\partial^2 U}{\partial q_1^2} & \frac{\partial^2 U}{\partial q_1 \partial q_2} & \cdots & \frac{\partial^2 U}{\partial q_1 \partial q_N} \\ \frac{\partial^2 U}{\partial q_2 \partial q_1} & \frac{\partial^2 U}{\partial q_2^2} & \cdots & \frac{\partial^2 U}{\partial q_2 \partial q_N} \\ \vdots & \vdots & \ddots & \vdots \\ \frac{\partial^2 U}{\partial q_N \partial q_1} & \frac{\partial^2 U}{\partial q_N \partial q_2} & \cdots & \frac{\partial^2 U}{\partial q_N^2} \end{pmatrix} \tag{4.2}$$

The Hessian matrix is the square matrix of second-order partial derivatives of the potential function. It describes the local curvature of the potential function.

The total kinetic energy of the system is given by a sum of the kinetic energies of all the atoms and it takes the form $T = (1/2)\dot{\mathbf{q}}^T\mathbf{M}\dot{\mathbf{q}}$, where a dot represents differentiation with respect to time. The classical Lagrangian is given by $L = T - U$ and using Hamilton's principle (or equivalently using Lagrange's equations), the well-known governing equations of motion $\mathbf{M}\ddot{\mathbf{q}}+\mathbf{H}\mathbf{q} = \mathbf{0}$ are obtained. Here M is the mass (or inertia) matrix. Looking for non-trivial synchronous motion of the form $q(t) = e^{i\omega t}u$ in a normal mode leads to the eigenvalue problem

$$\mathbf{H}\mathbf{u} = \lambda\mathbf{M}\mathbf{u}, \tag{4.3}$$

where $\lambda_i = \omega_i^2$ is the ith eigenvalue that represents the square of the natural frequency ω_i, and $\mathbf{u}_i$ is the corresponding eigenvector, for i =1,2,... 3N.

The Hessian matrix is positive semi-definite, and the eigenvalues extracted from it are all positive since they are associated with a positive semi-definite matrix of the vibrational frequencies (except for the first six

eigenvalues which are zero as they correspond to translational and rotational rigid body motions). However, because of the complexity of the potential energy landscape $U(\mathbf{q})$ in the space spanned by the general co-ordinates and limited numerical accuracy, it is very difficult to reach the global potential energy minimum while obtaining the equilibrium configuration of a group of atoms. This leads to computed Hessians that are not positive semi-definite. The eigenvalues obtained do not satisfy the requirement of being equal or greater than zero.

This problem has been reported before [120] and can be overcome using a technique called 'time averaged Hessian' [120], which was used here to address this. It basically consists in minimizing the potential energy as much as possible and subsequently performing a MD simulation of a thermal bath at very low temperatures. A Hessian $\mathbf{H}_k$ is calculated periodically while the MD trajectory is completed (resulting in a total number of K Hessians). The time averaged Hessian ($\bar{\mathbf{H}}$) is obtained by calculating the mean of every matrix component (one of such components is shown in Fig 4.2) among the K Hessians ($\bar{\mathbf{H}} = \frac{\mathbf{1}}{K} \sum_{k=1}^{K} \mathbf{H}_k$). Summarising, the steps taken in order to obtain the normal modes of a CNT using MD are:

1. Create nanotube geometry.
2. Minimise nanotube internal energy.
3. Run a 100 ps time-dependant simulation at 0.1°K and save positions every 1 ps.
4. Calculate Hessian $\mathbf{H}_k$ for all saved configurations.
5. Time-average the Hessians $\mathbf{H}_k$ created in step 4 to obtain $\bar{\mathbf{H}}$.
6. Extract all the eigenvalues and eigenvectors of the averaged Hessian

$\bar{\mathbf{H}}$ using equation (4.3).

7. Visualization of mode shapes (eigenvectors) associated with each normal mode.

For step 1, atom positions and bonds were created using Tubegen [121]. In step 2, a L-BFGS energy minimization algorithm [122] (an algorithm for quasi-Newton optimization) was used with GROMACS [39] in order to minimize the energy.

The input data required minor changes in the GROMACS force field file (addition of bare carbons). The time step for time integration was 0.001 ps, with a maximum number of steps to integrate of 100000. At this point, a typical value for the maximum force upon an atom in a nanotube is $F_{\max} = 5.557 \times 10^{-5}\text{kJmol}^{-1}\text{nm}^{-1}$ (1.6605×10^{-12}N).

For step 3 a Berendensen thermostat [123] is used. A number of 100 Hessians are computed in step 4. The final time averaged Hessian $\bar{\mathbf{H}}$ is obtained in step 5, and the eigenvalue problem was solved using Numeric Python [124] in step 6. The magnitude of the first six eigenvalues has been found to be below $10^{-2} \cdot \lambda_7$, where λ_7 is the smallest non-zero eigenvalue associated with oscillatory modes, i.e, the first six eigenvalues are effectively zero. Visualization of the mode shapes (step 7), given by the eigenvectors, was performed using Visual Python [125].

Gromacs parameter files are shown in Appendix B.

4.2 Results

We simulated a family of defect-free single walled CNTs of different length (L) to radius (R) ratios, ranging from long and narrow to the short and

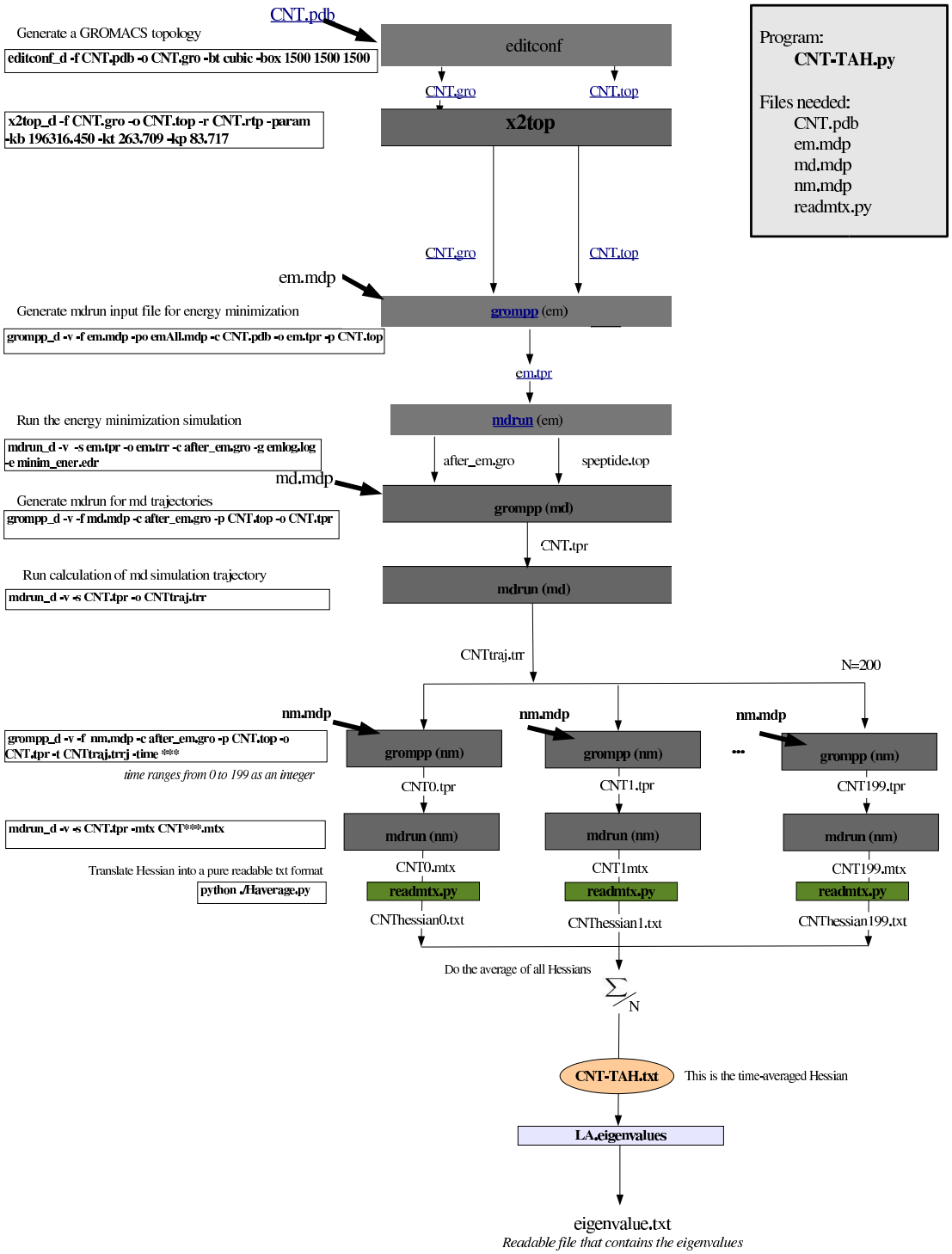

Figure 4.1: Simulation flowchart

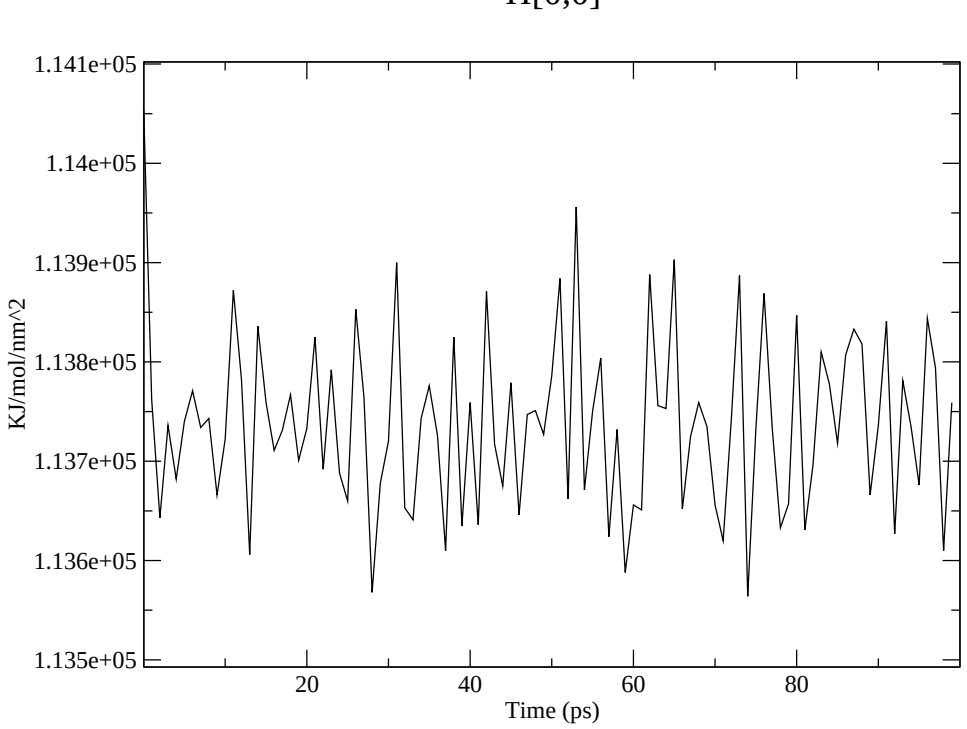

Figure 4.2: Temporal evolution of a typical diagonal entry of the Hessian matrix.

wide. This set of CNTs is displayed in Table 4.1.

4.3 Vibrational normal modes and the elastic properties of Carbon nanotubes

For each configuration shown in Table 4.1 we obtain a list of eigenvalues (squared frequencies) and eigenvectors (mode shapes), following the steps given in section 4.1. We sort the modes in order of increasing frequency. The calculated normal mode frequencies are presented in Fig. 4.3 for the CNT on row 1 and column D (denoted D1 in the future). Visualization of the eigenvectors, which correspond to the eigenmodes or normal modes obtained using Molecular Dynamics (MD), allow us to identify bending, twisting, stretching, breathing and radial modes, as well as thin shell modes, ring modes and other in-plane modes. They are shown for D1 in Fig. 4.4 The first six modes have a frequency of practically zero associated with rigid body motion. The ratio of the of the 7^{th} to the 6^{th} eigenvalue is over 600. This indicates that the small non-zero values of the first 6 eigenvalues are due to numerical reasons rather than physical. The six data correspond to 3 translations and 3 rotations of the overall CNT and would have a frequency of zero if it wasn't for numerical inaccuracies.

Modes 7 and 8 are the first bending mode (B1 in fig 4.4). The two frequencies are almost equal because they correspond to the same bending shape along two orthogonal planes parallel to the axis of the CNT.

Modes 9 and 10 are the second bending mode, mode 11 a twisting mode, mode 12 a stretching mode, and so on. As thin shell theory predicts, shell modes (including bending modes) come in doublets in our MD simulation. The frequencies in these doublets are slightly different due to the lack of

Table 4.1: The family of CNTs simulated. The nanotube configurations, labelled A-D for the columns and 1-5 for the rows. Within each column, the L/R ratio is approximately constant. Different rows correspond to different L/R ratios and columns represent number of atoms. Displayed in each box are numbers that define each CNT: the chiral vector (Ch), or "twist" of the nanotube [126], the length to radius ratio (L/R) and the number of atoms (N) in each pristine CNT. Note that the L/R ratio and the number of atoms depend on the chirality and cell counts.

	A	B	C	D
1		Ch=(3,3) L/R=1,208 N=24	Ch=(3,3) L/R=3.632 N=48	Ch=(3,3) L/R=23.006 N=240
2		Ch=(5,5) L/R=1.45 N=60		Ch=(5,5) L/R=25.126 N=720
3		Ch=(7,7) L/R=1.556 N=112	Ch=(7,7) L/R=4.144 N=252	Ch=(7,7) L/R= 26.69 N=1456
4	Ch=(10,10) L/R=0.362 N=80	Ch=(10,10) L/R=1.45 N=200	Ch=(10,10) L/R=3.986 N=480	
5	Ch=(50,50) L/R=0.508 N=1600			

cylindrical symmetry (the CNT is composed of a finite number of atom and thus cannot have continuous symmetry) and to the asymmetry introduced by computation. The frequency deviation between degenerated modes has an almost linear dependence on the mode number, as shown in Fig. 4.5. Many MD modes were easily identifiable, but some others are particularly challenging, such as those shown in Fig. 4.6, where a shear mode has the appearance of a bending mode. Because of this, we used a technique commonly used in Structural Dynamics called Modal Assurance Criterion [127] (MAC). It gives a quantitative estimate of the correlation between the shape of the simple beam Continuum Mechanics (CM) modes and the corresponding MD mode shape. For CM mode q_i and MD mode q_j, the correlation is given by the formula [127]

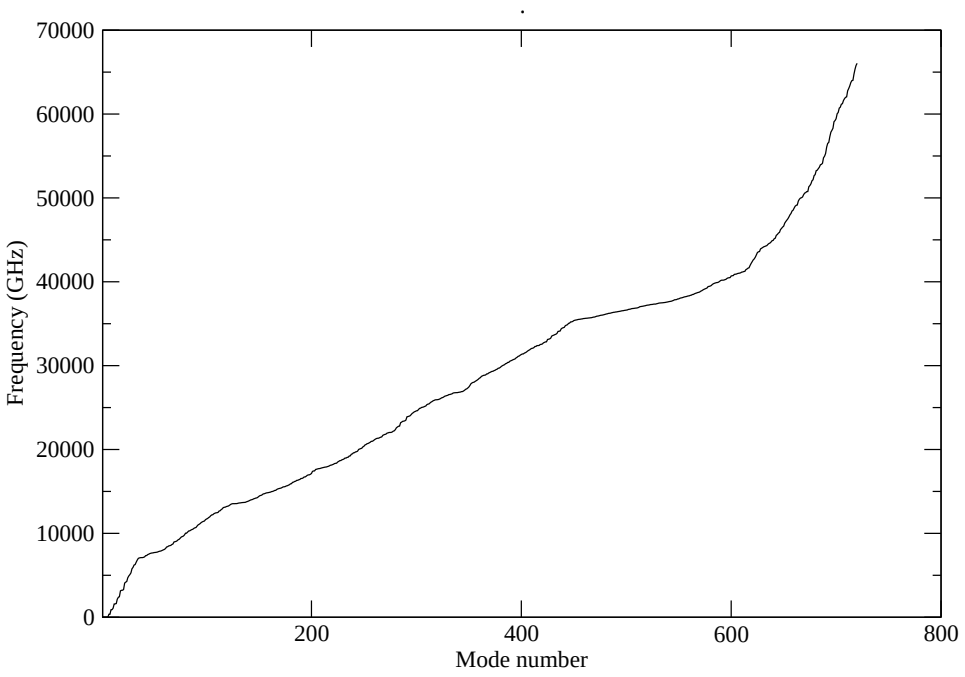

Figure 4.3: The complete set of eigenfrequencies of CNT D1, calculated with Molecular Dynamics as shown in Section 4.1

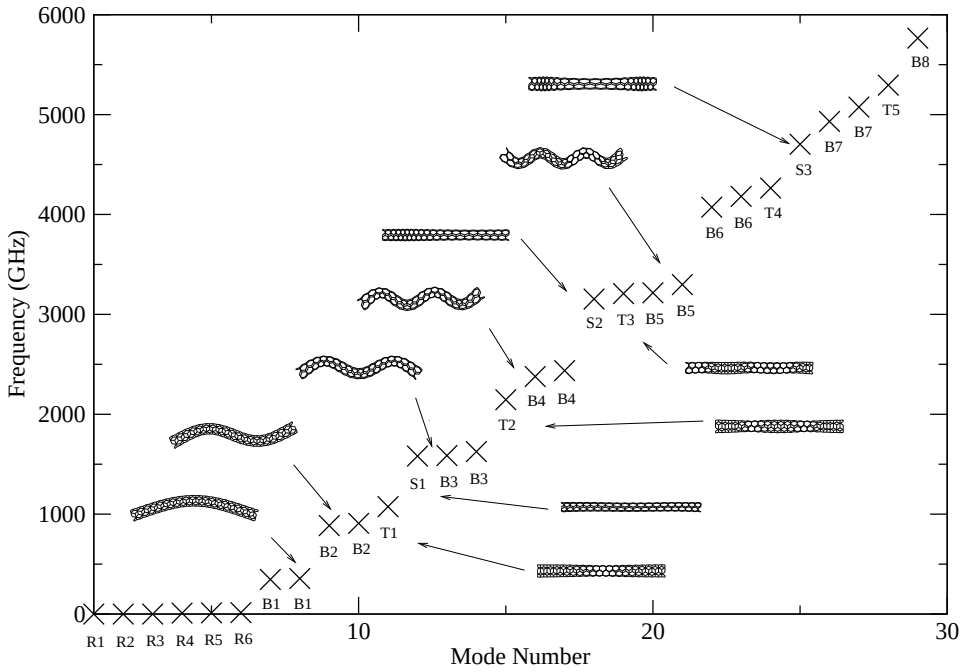

Figure 4.4: Zoom to the first 29 MD modes of CNT D1. Some bending (B), torsional (T) and stretching (S) eigenvectors are plotted (tube shapes). Rigid (R) modes have zero frequency of vibration.

$$C_{ij} = \frac{(|q_i^T q_j|)^2}{(||q_i||)^2(||q_j||)^2} \tag{4.4}$$

The correlation for CNT D1 is displayed as a graymap as shown in Figure 4.7. We note that the correlation is good for the first modes, although it drops progressively with the mode number. Direct visual inspection has shown us shell-twisting, shell-stretching and breathing-stretching mode couplings at the points where the MAC correlations vanishes, after the ninth bending mode.

Soedel's formula [114] for thin shells is optimised for bending modes through the use of beam functions. Because of this, we chose the bending modes as our main tool to demonstrate the accuracy of the different contin-

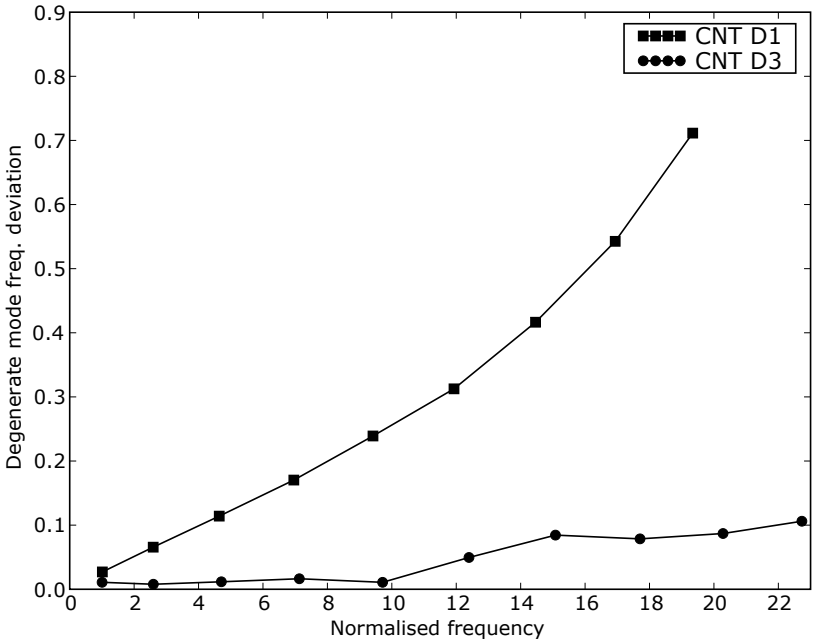

Figure 4.5: Normalised frequency deviation of the degenerate bending modes (D_d) versus normalised frequency ($\widetilde{f}$) for CNTs D1 and D3, where $D_g = \widetilde{f}_b(i) - \widetilde{f}_a(i)$, $\widetilde{f} = f/f_0$, i is the bending mode number and f_0 is the first non normalised bending frequency.

uum theories described, although stretching and torsional modes (uncovered by thin shell models) are also studied. The nanotubes selected for the study are CNTs D1-D3 (slim) and CNTs C1-C3 (stubby) because both pairs have CNTs with similar geometries although substantially different number of atoms.

A comparison of frequencies of the long-wave eigenmodes computed using MD simulations, and three analytical models (E-B, Timoshenko and Thin Shell) of different complexities was made for CNTs D3 and D1. Frequencies for CNT D3 are plotted in Fig. 4.8 while CNT D1 is shown in Fig. 4.9. We

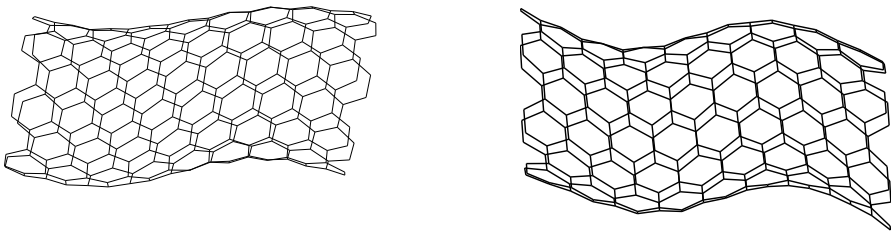

Figure 4.6: Left: mode produced by shear of the cross-section of CNT C3, at $f = 2694.11$ GHz. Right: second bending mode of CNT C3, at $f = 3080.05$ GHz.

can clearly see in this figure that the best fit for the molecular data is given by the thin shell case, followed by Timoshenko and Euler-Bernoulli. In all cases, the deviation increases with the frequency. The frequency mismatches shown are much higher than those appearing in classical beam and shell experimental setups [115]. This points out that the main source for the frequency error is the lack of discreteness in the continuum models.

It is interesting that the Timoshenko and thin shell frequencies seem to be lower than the MD frequencies. This seems to be in contradiction with Rayleigh's theorem, which states that increasing the degrees of freedom always decreases the frequencies. The reason we can guess for this behaviour is that we have modeled Timoshenko and Thin shell shapes that MD cannot imitate at a low energy cost, such as the perfect ends of a cylinder or the

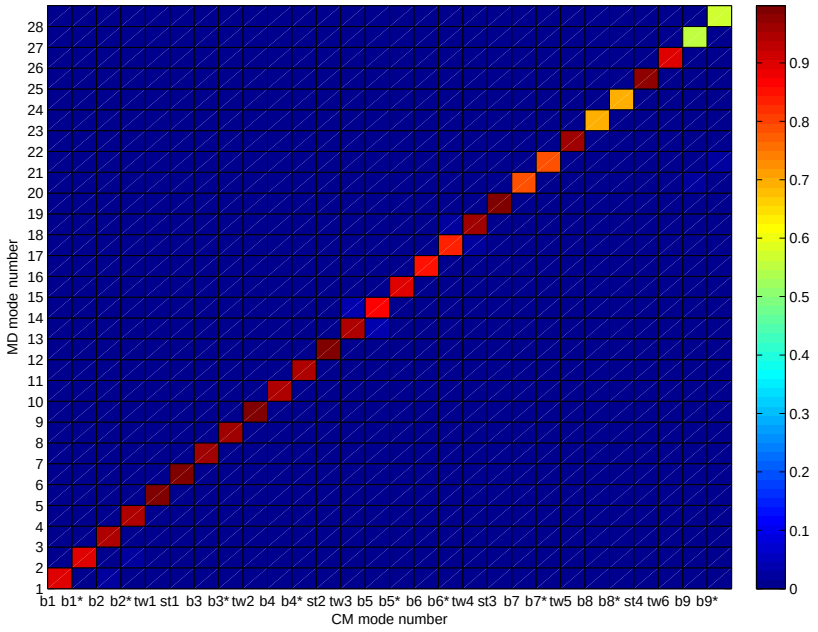

Figure 4.7: MAC color map showing the correlation between MD and CM bending (B), twisting (T) and stretching (S) eigenvectors for the first 28 modes of CNT D1.

constant cross-sectional area. This reasoning is specially applicable to the thin shell case, since an energy minimization approach is used [128] (the Galerkin method) when obtaining Soedel's frequencies (eq. 3.48).

A specially useful output is the first bending eigenfrequency of a given nanotube, as we can calculate from this eigenvalue the CNT wall thickness. The procedure for its calculation is shown in the next section. From it, the wall thickness $h = 0.13185$ nm of CNT D3 is obtained, in agreement with previous studies [129].

In order to see how the different CM theories hold up at other L/R ratios, a comparison of frequencies of the long-wave eigenmodes using MD simulations and three analytical models(EB, Timoshemko, Thin Shell) for

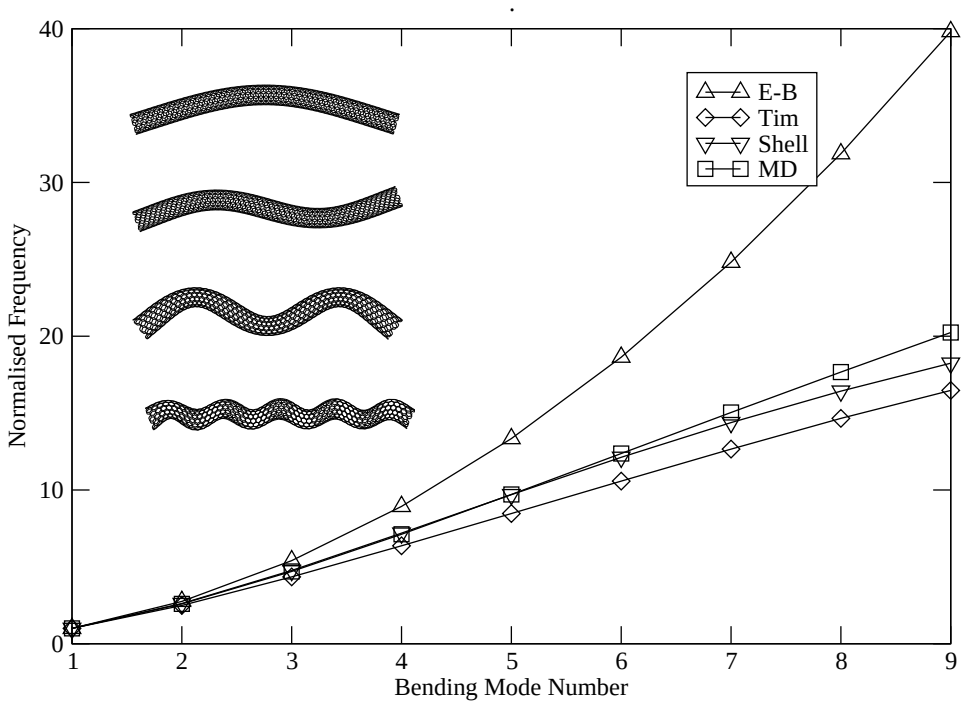

Figure 4.8: Euler-Bernoulli (EB), Timoshenko (Tim), Thin Shell(Shell) and Molecular Dynamics (MD) normalised bending frequencies ($\widetilde{f} = f/f_0$) for nanotube D3. Top left: side view of MD bending modes number 1, 2, 3 and 9.

nanotubes C3 and B3 instead of nanotubes D1 and D3, is shown in Fig. 4.14. The same behaviour is observed, although EB frequency deviation is more significant because shear effects are not negligible in beams that are stubby, and the E-B theory does not account for such shear deformation.

We have also compared data from CM formulas for stretching and twisting modes with our MD data. The order in which extensional and torsional modes appear (as singlets) depends on the aspect ratio (L/R) of the nanotube. Their frequency ratios also start to depart from the ratios predicted by simple beam theory. This ratios from simple beam theory are the natural numbers, and the deviation is shown in Fig. 4.10 for CNT D1 and in

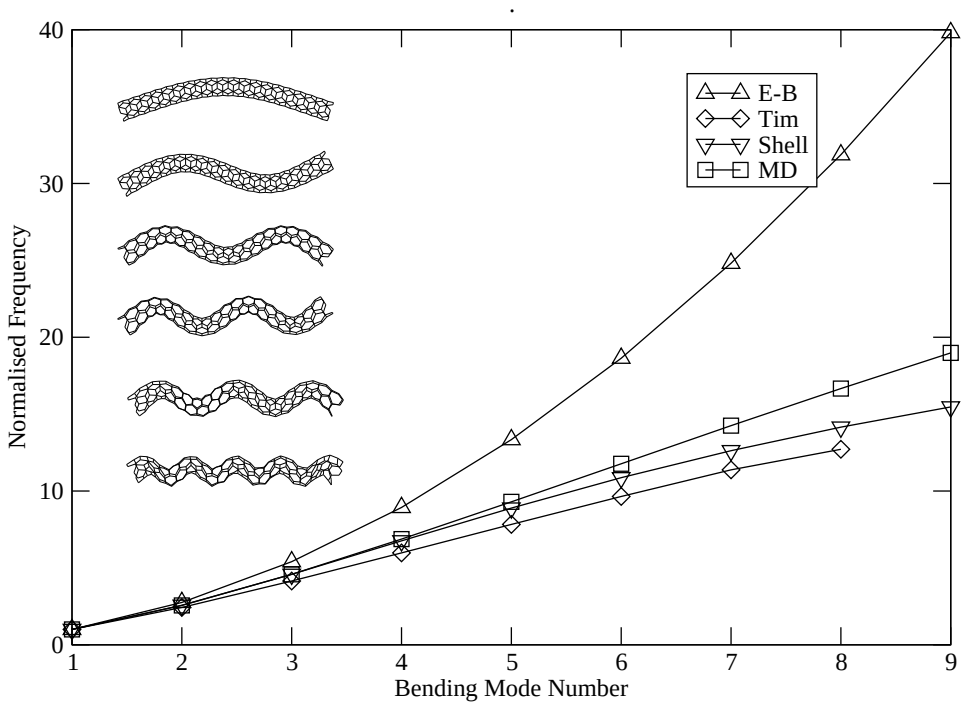

Figure 4.9: Same as FIG. 4.8, for nanotube D1. Top left: Side view of MD bending modes 1, 2, 3, 4, 5 and 9.

Fig. 4.11 for nanotubes D3. The frequency deviation for extensional and torsional modes is significantly smaller than the frequency deviation corresponding to bending modes.

As it is shown in Figs. 4.8-4.11, continuum models fail to predict mode ratios at high frequencies for the CNT system studied here. The values of the allowed modes diverge substantially as the characteristic length in the (i) axial and (ii) radial direction progressively shortens, thus violating the assumptions of the continuum theories used. A substantial amount of the frequency divergence of the CM modes is due to the assumptions made by these models.

The frequency deviation percentage of the different continuum theories

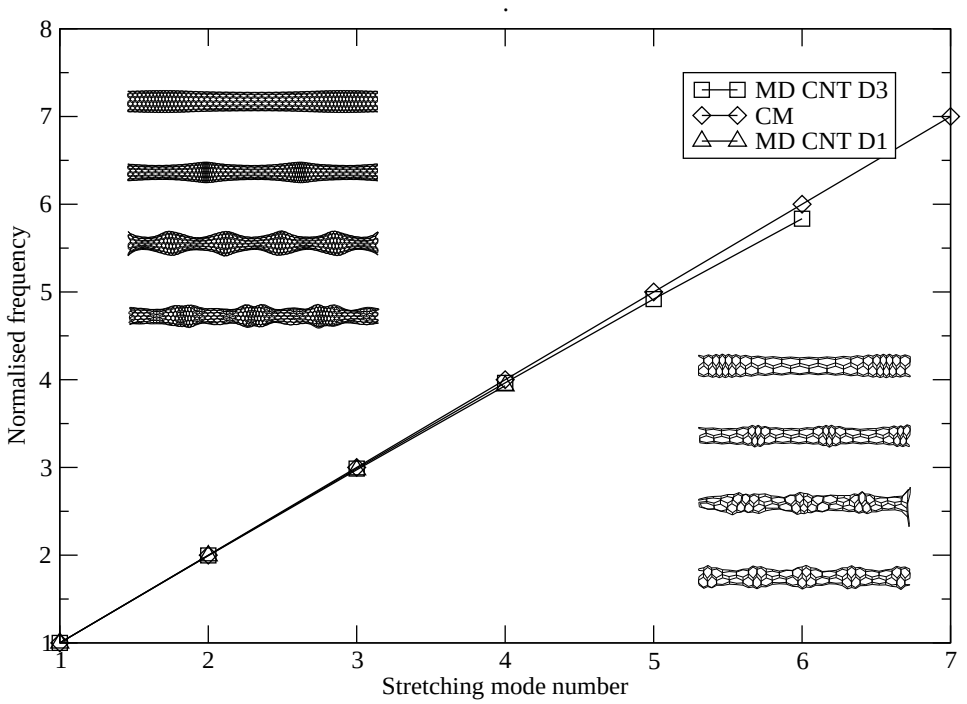

Figure 4.10: Stretching modes normalised frequencies. Top left: stretching shapes of modes 3, 5, 7 and 9, CNT D3. Lower right: stretching modes 3, 5, 7 and 9, CNT D3.

from the MD data has been obtained for each of the CM models used, and are plotted in Fig. 4.12, for nanotubes D1 and D3. Using elementary calculus (quadratic curves fitted to the deviation midpoints), an approximate scaling expression of the deviation ε for the ith bending modes is obtained. For CNT D1,

$$\varepsilon_{\mathrm{EB}} \simeq 1.72 i^2 \tag{4.5}$$

$$\varepsilon_{\mathrm{TIM}} \simeq -0.47 i^2 \tag{4.6}$$

$$\varepsilon_{\mathrm{SHELL}} \simeq -0.29 i^2. \tag{4.7}$$

For CNT D3,

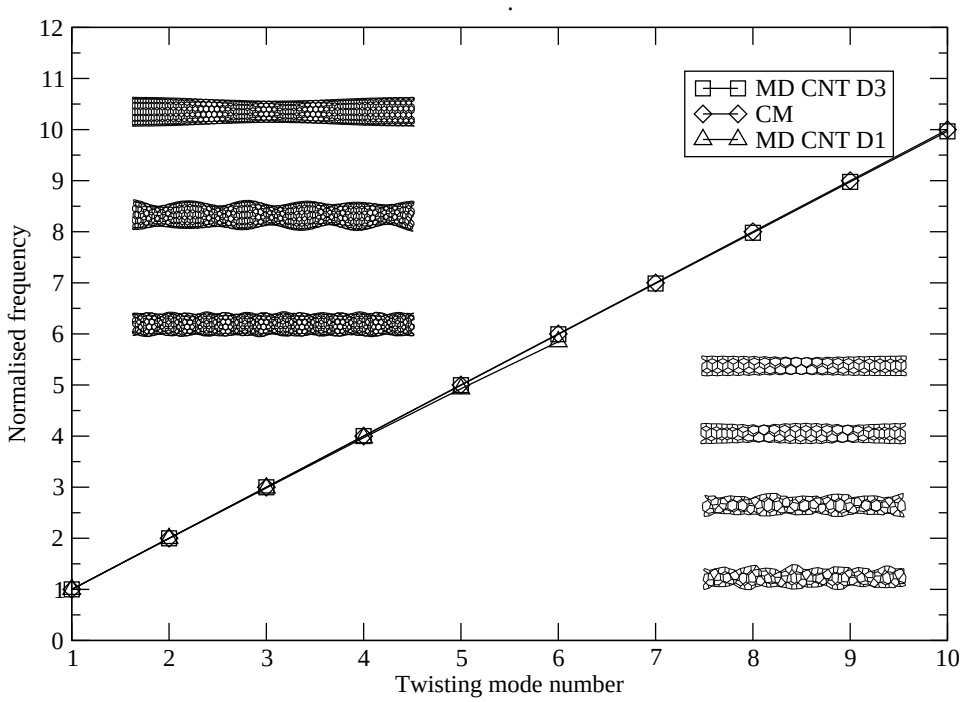

Figure 4.11: Twisting modes normalised frequencies. Top left: twisting shapes of modes 1, 5 and 14, CNT D3. Bottom right: twisting modes 1, 2, 6 and 9, CNT D1

$$\varepsilon_{\mathrm{EB}} \simeq 1.52 i^2 \tag{4.8}$$

$$\varepsilon_{\mathrm{TIM}} \simeq -0.28 i^2 \tag{4.9}$$

$$\varepsilon_{\mathrm{SHELL}} \simeq -0.16 i^2. \tag{4.10}$$

Note that the different frequency deviations between CNT D1 and CNT D3 among the same MD model can only be due to the different number of atoms. It is an explicit manifestation of their different discreteness. The thin shell model has the lowest deviations, and is less influenced by the number of atoms. In this sense, the thin shell model is the most robust.

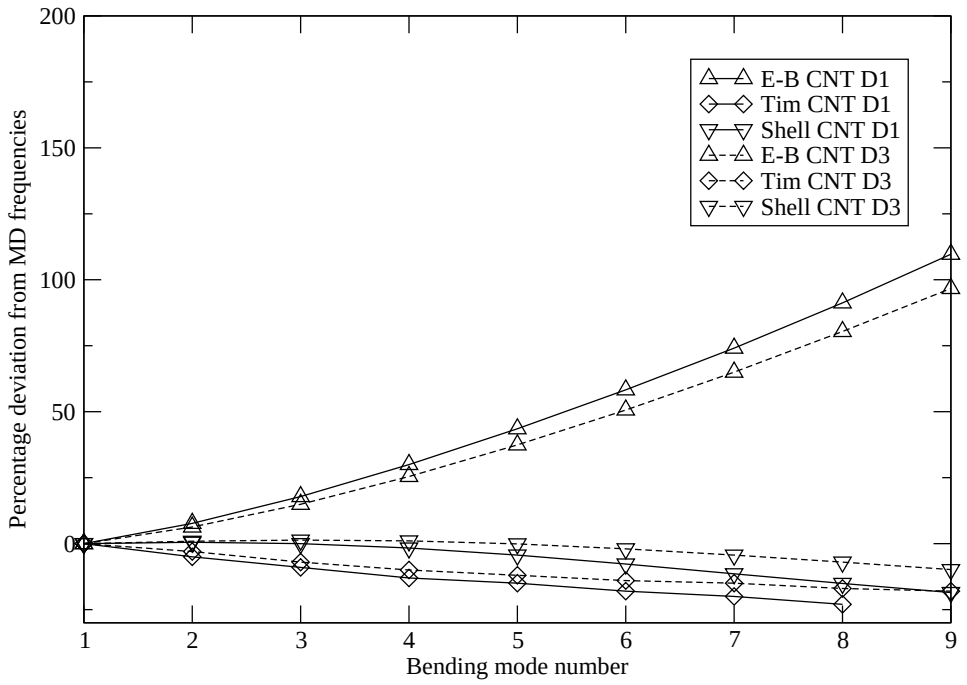

Figure 4.12: Deviation (D) of the EB, TIM and Shell normalised frequencies from MD normalised frequencies. For EB, $D = (\widetilde{f}_{\mathrm{EB}} - \widetilde{f}_{\mathrm{MD}})/\widetilde{f}_{\mathrm{MD}}$. Analogous for Timoshenko and Shell deviations.

4.4 Calculation of SWCNT wall thickness h

There is currently a debate about the value of the wall thickness of CNTs. From a CM point of view, the wall thickness is an important value for the CNT frequency calculations. This is a difficult thing to attempt since there is no 'wall', but wavefunctions that decay exponentially away from the CNT and never reach zero value. In order to calculate the wall thickness h of CNT D3 using our results we follow the procedure below:

1. Extract the value of EI from the equality $\omega_1^{\mathrm{EB}} = \omega_1^{\mathrm{MD}}$, being I the second area moment of inertia of a tube.

2. Get from the literature a value for the Young's modulus E_{lit} to get I

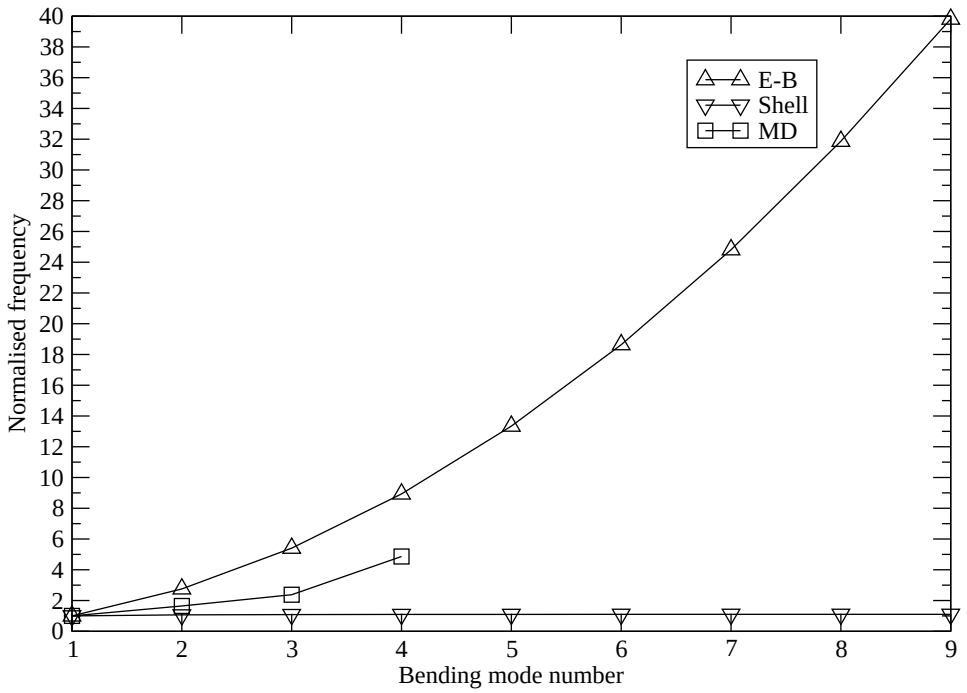

Figure 4.13: Bending normalised freqs, nanotube B3.

using the previous step. Extract h and compare it with literature

For step 1, since we have the eigenvalues of a non mass-weighted Hessian matrix in GROMACS units (refer to manual [39]), and converting to S.I. units:

$$\omega_1^{\mathrm{MD}} = \sqrt{\lambda_1^{\mathrm{MD}}} = \sqrt{\frac{5.94902}{12.01}\left[\frac{\mathrm{a.m.u}\cdot\mathrm{rad}^2\cdot\mathrm{ps}^{-2}}{\mathrm{a.m.u}}\right]} = 112.01\mathrm{GHz} \qquad (4.11)$$

On the other hand, $\omega_1^{\mathrm{EB}} = \omega_1^{\mathrm{EB}^*}\cdot((EI)^{1/2}ML^3)^{-1/2}$, where L is the length of nanotube D3, $L = 12.92$ nm, and M the mass mass of nanotube D3, $M = N_{C^{12}}\cdot M_{C^{12}}/N_A = 2.903713\cdot 10^{-23}$Kg, being N_A the Avogadro's number, $N_{C^{12}}$ the number of atoms in nanotube D3 and $M_{C^{12}}$ the mass of a carbon atom in atomic units. $\omega_1^{\mathrm{EB}^*} = 22.37502486$ is the first non-dimensionalised, non-normalised Euler-Bernoulli frequency: $\omega_1^{\mathrm{EB}^*} = \zeta^2$, be-

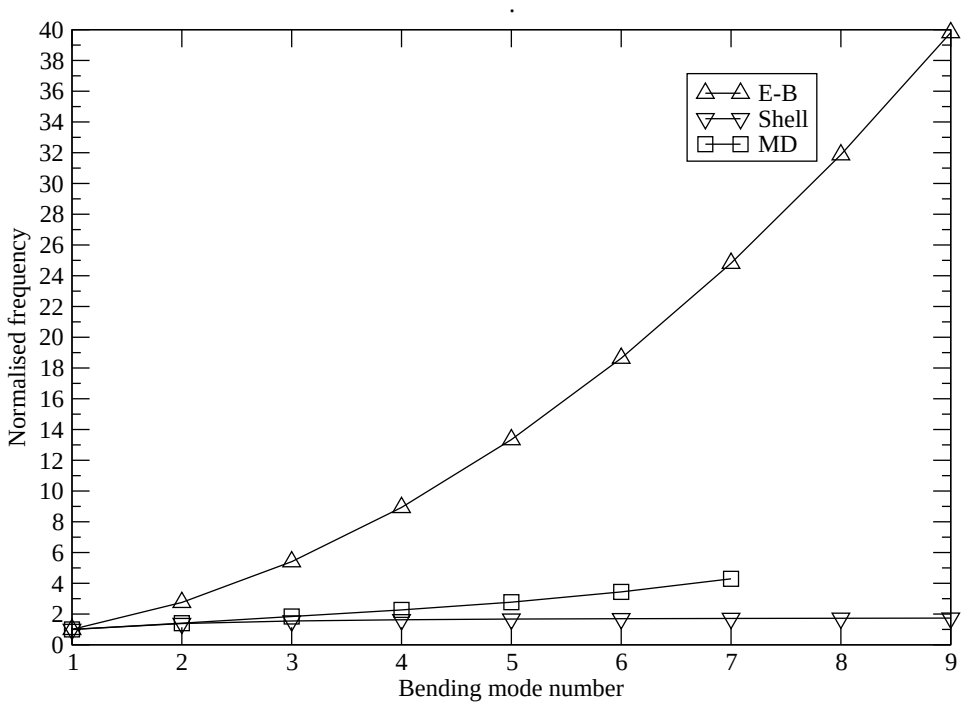

Figure 4.14: Bending normalised freqs, nanotube C3

ing ζ the first solution of the non-normalised Euler-Bernoulli equation. We can therefore extract $EI = 6.196074036 \cdot 10^{-26}\text{Kg} \cdot \text{m}^3\text{s}^{-2}$.

For step 2, we refer to [129], where a list of reported values for E and h is given. Setting, for example, $E_{\text{literature}} = 1.238\text{TPa} = 1.238 \cdot 10^{12}\text{Kg} \cdot \text{m}^{-1}\text{s}^{-2}$, then $I = \frac{EI}{E_{\text{literature}}} = 5.00490633 \cdot 10^{-38}\text{m}^4$.

The cross-section of a tube is a ring, so $I = \frac{\pi}{4}(r_2^4 - r_1^4)$, where r_1 is the inner radius and r_2 is the outer radius of the single walled nanotube. If we call r the mean radius of the tube (known), $r = 4.915 \cdot 10^{-10}\text{m}$, then $r_1 = r - h/2$ and $r_2 = r - h/2$. For simplicity, we name $a = h/2$ so that we obtain the equation

$$(r + a)^4 - (r - a)^4 = 4I/\pi \tag{4.12}$$

Using the bisection method we arrive at the solution $a = 6.5925043 \cdot 10^{-11}$ m and therefore the nanotube wall thickness is $h = 2a = 0.13185$ nm, which is on the range of the thicknesses presented in the cited paper [129].

4.5 The combination of Rayleigh's method with molecular dynamics

The computationally expensive part of the procedure of extracting the eigenmodes of a vibrating CNT is the solution of the eigenvalue problem. However, since we know that the low frequency mode resemble the continuum modes, this information can be incorporated profitably to reduce the computational time while using the detailed molecular dynamics generated Hessian and still avoiding the complete eigensolution.

In order to have a quantitative estimate for the reasons as to why the EB frequency differ from MD calculations deviations, we built models of nanotubes by placing their atoms the way the EB theory predicts (we called it the EBMD model).

This could be achieved by employing Rayleigh's method of the assumed modes. The method has the basis that the eigenvalues calculated from the Rayleigh's quotient are an order more accurate that the accuracy of the assumed eigenvectors.

By comparing the EB, EBMD and MD frequency curves, we are able to have a quantitative estimate of the amount of deviation caused by (i) the EB assumption of normals remaining normal after deflection and (ii) the rest of the assumptions. The effect of lack of homogeneity will be measured by comparison of the curves of nanotubes with different atom density for a given R/L ratio (CNTs D1 and D3).

The procedure is in the spirit of the Rayleigh variational principle applied

to the detailed Lagrangian of MD in conjunction with assumed continuum modes.

The Rayleigh-Ritz method states that any constrained shape will always give a value of the potential energy that is equal or greater than the ground-energy. The Rayleigh's quotient of the constrained shapes are given by

$$\left(\frac{\mathbf{q}_{\text{const}}^{\mathbf{T}}\mathbf{H}\mathbf{q}_{\text{const}}}{\mathbf{q}_{\text{const}}^{\mathbf{T}}\mathbf{M}\mathbf{q}_{\text{const}}}\right)^{1/2} \tag{4.13}$$

In order to build the normalised frequency curves for the EBMD nanotube, we proceeded through the following steps:

1. Get the energy-minimised nanotube from GROMACS.

2. Build the shape of the constrained CNT by imposing the Euler-Bernoulli constraints ('normals remain normal' after deflection) through the transformation formula [130]. If z is the principal axis of the CNT, then the displacement of an atom of the E-B deformed nanotube is given by

$$q_x = 0 \tag{4.14}$$

$$q_y = w_i^{\text{EB}}(z) \tag{4.15}$$

$$q_z = -y\frac{\partial w_i(z)}{\partial z} \tag{4.16}$$

$$\tag{4.17}$$

and the new generalised coordinates for each atom are

$$q_i = (q_{ix}, q_{iy}, q_{iz}), \qquad i = 1..N \tag{4.18}$$

Note that $w_i^{\text{EB}}(z)$ is the deflection of the center line of a free-free Euler-Bernoulli beam, for mode number i [131]:

$$w_i^{\mathrm{EB}}(z) = A\left(\cosh\beta_i z - \frac{\sinh\beta_i L + \sin\beta_i L}{\cosh\beta_i L - \cos\beta_i L}(\sinh\beta_i z + \sin\beta_i z)\right) \quad (4.19)$$

where

$$\beta_i^2 = (m/EI)^{1/2} \cdot \omega_i^{\mathrm{EB}} \quad (4.20)$$

and A ia an arbitrary amplitude constant.

3. Calculate the new normalised eigenfrequency associated to the transformation, for each bending mode number, using Rayleigh's method

$$\omega_{\mathrm{EBMD}} = \left(\frac{\mathbf{q}_{\mathrm{const}}^{\mathbf{T}}\mathbf{H}\mathbf{q}_{\mathrm{const}}}{\mathbf{q}_{\mathrm{const}}^{\mathbf{T}}\mathbf{M}\mathbf{q}_{\mathrm{const}}}\right)^{1/2} \quad (4.21)$$

A similar approach was taken in order to build continuum mechanics-molecular dynamics models for torsional and stretching modes, and they are used on the MAC. The atoms of CNTs D1 and D3 were placed on the positions that the CM theory predicts, and these mode shapes were used for the twisting and stretching CM shapes used on the MAC plot in the previous chapter.

Prior to the analysis of the EBMD curves, we note that two cases are possible:

- If the EBMD frequency curve is close to the E-B curve, that would mean that the frequency difference between the E-B and MD curves is due to the condition of normals remaining normal during deflection.
- If the EBMD frequency curve is close to the MD, that would mean that the frequency difference between the E-B and MD curves is not due to the condition of normals remaining normal during deflection, but to any other reason.

On the EBMD hybrid graph of CNT D1 and D3 for bending modes (Figs. 4.15 and 4.16) we observe that the EBMD frequency curve lies approximately between the MD and E-B curves. We get the conclusion that, although the condition of normals remaining normal after deflection significantly contributes to the frequency deviation, other factors are also important (loss of homogeneity, shear effects, irregularities in nanotube ends, etc).

We also observe that the EBMD curve on Fig. 4.16 (CNT D3) is closer to the E-B curve than of Fig. 4.15 (CNT D1). This means that, given a length to diameter ratio, the fewer atoms a CNT has, the more important the E-B constrains are on the frequency deviation from the MD data. Again, this is a manifestation of the contribution of the number of atoms to the frequency deviation of the continuum models.

4.6 Time domain simulation of vibration of CNTs

For data corroboration, we used a novel approach by comparing the CM normal mode frequencies with the spectra of the nanotube, calculated with molecular dynamics. The Fourier signal analysis represents a powerful tool for obtaining the characteristic frequencies of vibration of a CNT, taking the atom position on a CNT as it fluctuates with time as the signal for the analysis.

We run a MD simulation in which the trajectories of selected atoms were recorded during a Berendensen thermal bath [123]. The bath acts as a source of thermal energy, adding or removing heat from the system introducing the possibility to change atomic velocities at each step. The rate of change of temperature is proportional to the difference in temperature between the bath and the system.

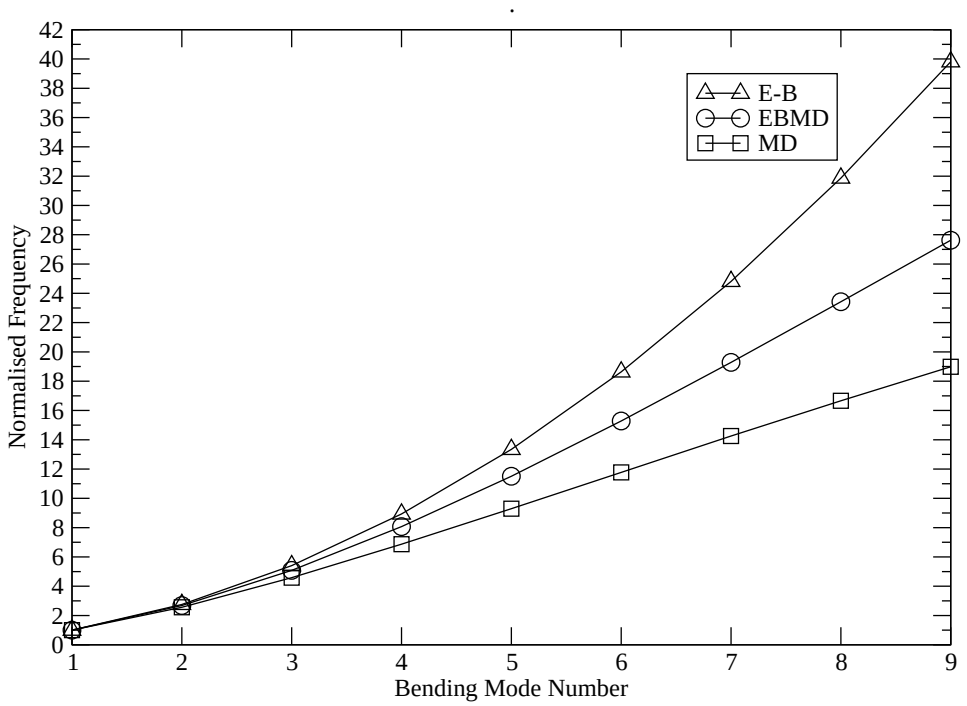

Figure 4.15: CNT D1 normalised frequencies for the Euler-Bernoulli (E-B),model, the Molecular Dynamics (MD) model and those obtained by imposing the Euler-Bernoulli condition to the molecular dynamics model (EBMD).

The position of the x coordinate of atom 0 (located at one end of CNT D1) was recorded every 0.0005 ps. With a sampling frequency of $f_s = 2000$ THz we captured even the highest natural vibrations, corresponding to mode number 720, $f_{720} = 194.2$ THz.

We recorded 131072 samples, giving a total sampling time of $T_s = 65.536$ ps, several times higher than the vibration period of the lowest frequency mode ($f_1^{-1} = (7.03803 \cdot 10^{11}/(2\pi))^{-1} = 8.927$ ps), and a frequency resolution of $\Delta_f = 1/T_s = 15.2588$ GHz. The temperature coupling of the thermal bath was set to $\tau = 0.1$.

Fig. 4.17 clearly shows peaks at the normal mode frequencies: ratios

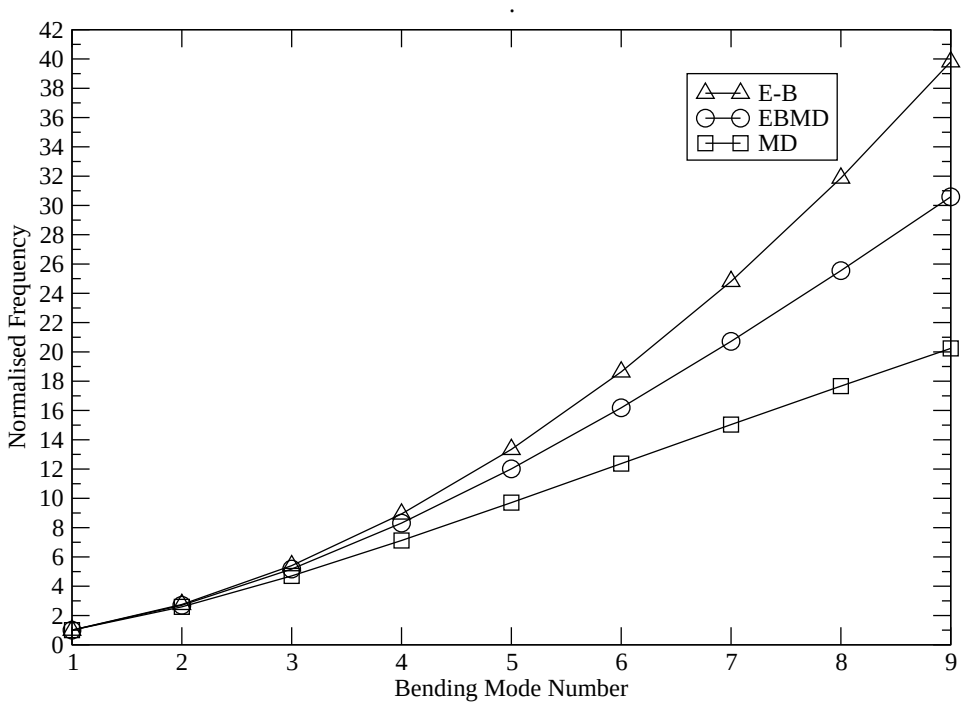

Figure 4.16: Left: CNT D3 normalised frequencies for the Euler-Bernoulli (E-B) model, the Molecular Dynamics (MD) model and those obtained by imposing the Euler-Bernoulli condition to the molecular dynamics model (EBMD).

between the FFT's peaks are similar to E-B ratios and even closer to Timoshenko's, thin shell or the MD frequencies obtained via the eigenvalue problem of the time averaged hessian matrix. The same procedure was taken to find matches between stretching frequencies, by calculating the PSD of the z component of the same atom (Fig. 4.17). The match between different models is even higher that in the bending case. Table 4.2 shows the absolute bending and stretching frequencies for CNT D1.

We also checked the stability of the resonant frequencies for different temperatures. We used the above procedure for a range of temperatures ($T = 0.001, 4, 20, 40, 500°\mathrm{K}$). It can be seen in Fig. 4.19 that these eigenfre-

m	EB	Tim.	Shell	MD	PSD	CM	MD	PSD
1	355.3	355.3	355.3	355.3	366.2	1581.75	1581.75	1602
2	979.34	932.37	914.25	909.38	930.8	3136.5	3153.42	3159
3	1919.78	1725.54	1629.20	1629.18	1633	4745.25	4703.21	4715
4	4740.48	2676.64	2401.36	2441.88	2457	6327	6217.63	6241
5	6621.41	3741.20	3159.62	3302.84	3311	7908.75	7662.87	7675
6	8815.87	4885.02	3860.74	4183.33	4196	9490.5	9041.96	9064

Table 4.2: Left: absolute Euler-Bernoulli (EB), Timoshenko (Tim.), Thin Shell (Shell), Molecular Dynamics normal mode (MD) and Power Spectrum Density (PSD) bending frequencies (MD) for CNT D1. Right: absolute Continuum Mechanics (CM), MD and PSD stretching mode frequencies (GHz) for the same nanotube. m denotes the bending and stretching mode number.

quencies do not vary throughout the temperatures.

4.7 Thermal properties of carbon nanotubes

Similar to electronic properties, thermal properties of carbon nanotubes (CNTs) become more important in theoretical research and applications recently. It is found that thermal properties of CNTs not only show unique and significative low dimensional features but also play critical roles in controlling the performance and stability of CNT based devices because of the key problem of energy dissipation and thermal transport [132].

Specific heat capacity, also known simply as specific heat, is the measure of the heat energy required to increase the temperature of a unit quantity of a substance by a certain temperature interval.

We extend the molecular structural mechanics approach to the study

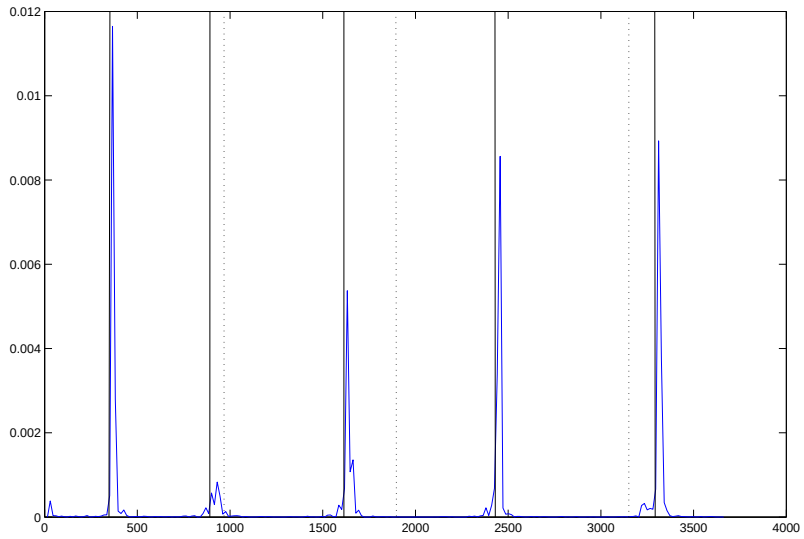

Figure 4.17: Power density spectrum of the lowest frequencies at $T = 40°$K, for CNT D1. Note the resemblance to EB (dotted vertical lines) and TAH-MD (straight vertical lines) eigenfrequencies.

of the specific heat of carbon nanotubes by introducing our frequency data into equation 4.19. The vibrational modes of the nanotube are quantized according to the theory of quantum mechanics. The specific heat of a single-walled carbon nanotube is calculated and the temperature dependence of the specific heat is demonstrated.

The heat capacity at constant volume is defined as $C_v = \left(\frac{\partial U}{\partial T}\right)_V$ where U is the energy and T the temperature. The contribution of the phonons to the heat capacity of a crystal is called the lattice heat capacity and is denoted by C_{lat}

The total energy of the phonons at a temperature $\tau(= k_B T)$ in a crystal may be written as the sum of the energies over all phonon modes:

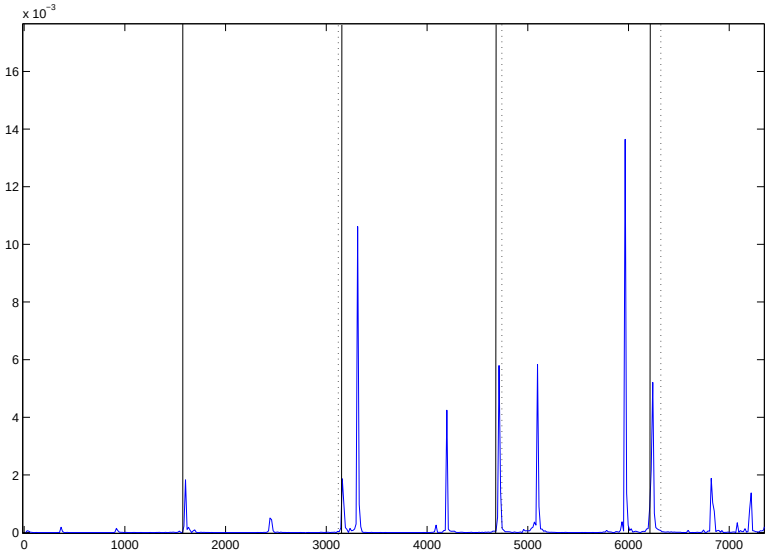

Figure 4.18: Power density spectrum for movement of atom 0 along the axis of CNT D1, $T = 20°$K. Again, peaks appear near the CM and even closer to the time averaged hessian predicted eigenfrequencies.

$$U = \sum_K < n_K > \hbar\omega_K \tag{4.22}$$

where $< n_K >$ is the thermal equilibrium occupancy of phonons of wavevector K, and is given by Plank's black body distribution

$$< n >= \frac{1}{\exp(\hbar\omega/\tau) - 1} \tag{4.23}$$

The lattice vibrational energy can then be expressed as [133]:

$$U = \sum_K \frac{\hbar\omega_K}{\exp(\hbar\omega_K/\tau) - 1} \tag{4.24}$$

The specific heat is found by differentiating the internal energy with

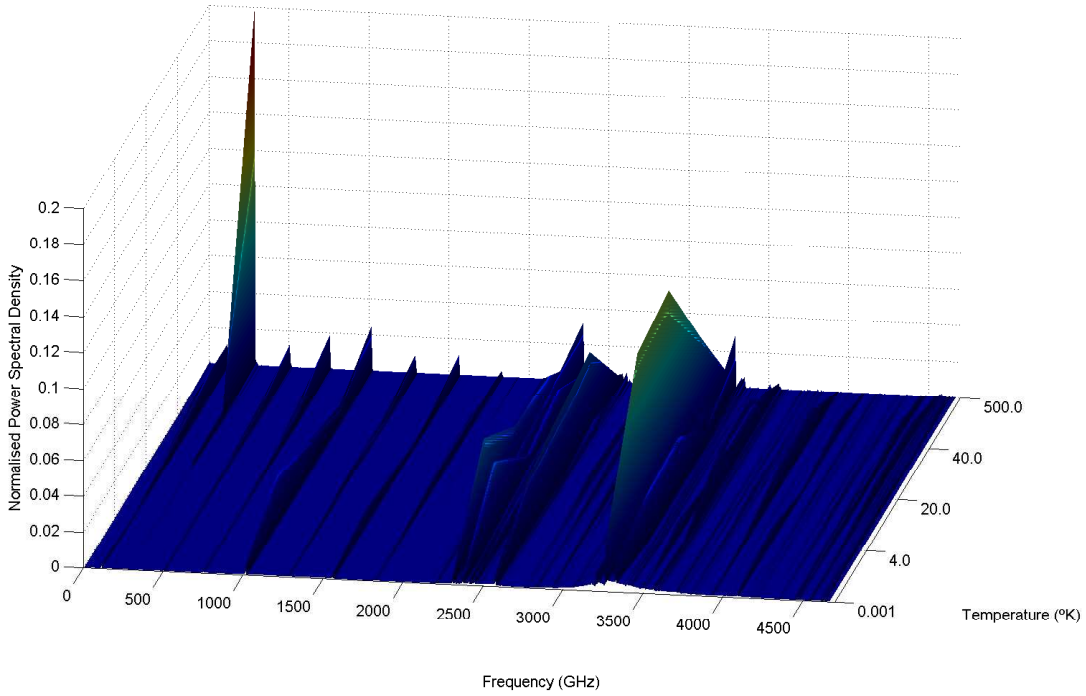

Figure 4.19: : Power density spectrum for atom 0 during a 4.1943 ns, $T = 0.001, 4, 20, 40, 500^{\circ}$K as a color map.

respect to the temperature:

$$C_V = k_B \sum_{j=1}^{3n} \frac{(\hbar\omega_j/k_BT)^2 exp(\hbar\omega_j/k_BT))}{(exp(\hbar\omega_j/k_BT) - 1)^2} \tag{4.25}$$

We extend the molecular structural mechanics approach to the study of the specific heat of carbon nanotubes. The temperature dependence of the specific heat is shown in Fig. 4.20, where specific heat approaches the Dulong and Petit's value of $N \cdot 3k_B$ [134] as the temperature increases. Also, the curve is cubic for low temperatures and linear for mid temperatures, in agreement with previous experiments [135] and calculations [136, 137].

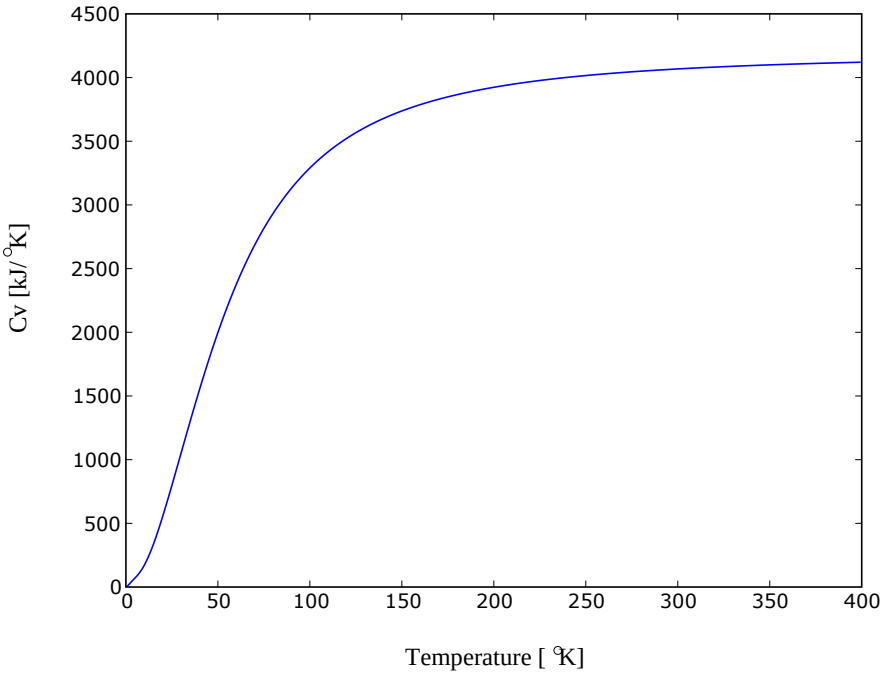

Figure 4.20: Specific Heat of CNT D1 as a function of temperature.

Chapter 5

Conclusions and future work

Summarising, we have obtained the complete set of Molecular Dynamics normal modes of thousand-atom carbon nanotubes. A systematic comparison with some of the most important and continuum theories has proven that continuum methods fail significantly as the mode number increases and as the number of atoms decreases.

We have inferred an expression law for the frequency deviation of continuum mechanics modes from molecular dynamics modes, a correction that can be applied to recently published papers ([36], [138]). We have elaborated a frequency correction formula for the Euler-Bernoulli, Timoshenko and Thin Shell frequency formulas.

Our calculation of the nanotube wall thickness h from our novel MD frequencies shreds light into the current debate about the thickness value, and the wall thickness we obtained ($h = 0.617\mathring{A}$) is in agreement with other studies.

We developed a new model from the combination of the Euler-Bernoulli beam theory with Molecular Dynamics. It has let us identify that the causes for the deviation between the Euler-Bernoulli and Molecular dynamics fre-

quencies. It has shown that the condition of 'normals remaining normal after deflection' significantly contributes to the divergence, but it has also been proved that other factors such as the number of atoms are important.

Also, the MAC technique has been used for the first time on the nanoscale. It effectively shows at a glance the correlation between continuum mechanics mode shapes (eigenvectors) and their Molecular Dynamics counterpart.

We double-checked our results with the frequency peaks on the power density spectrum arising from the Fourier transform of the atom displacements during thermal baths across a range of temperatures. A power spectral density (PSD) analysis was used to corroborate the normal mode frequencies (E-B, Timoshenko, Thin Shell and Molecular Dynamics), showing the same divergences that those previously shown. Also, the resonant frequency peaks in the PSD results show excellent stability across a range of temperatures.

Finally, the specific heat capacity was calculated for the first time using all the MD eigenfrequencies, showing agreement with previous observations.

For future work, it would be desirable to build an algorithm for calculating the eigenmodes and eigenfrequencies analytically, because it would improve the time to compute the modes by a factor of 100 (as it would be necessary to calculate 100 Hessians and then average them). The procedure for building this algorithm is presented in Appendix A.

It would also be interesting to extend our study to other carbon nanostructures such as nanotube Y-junctions and carbon supernanotubes, a structure of welded nanotubes that resembles itself to another nanotube.

The normal modes of vibration seem to play an important role on the superconductivity on carbon nanotubes. Calculating the conductivity of a CNT at different frequencies of vibration may contribute to understand this

physical phenomenon.

Bibliography

[1] H W Kroto, J R Heath, S C OBrien, R F Curl, and R E Smalley. C60 buckyminsterfullerence. *Nature*, 318:162, 1985.

[2] R B Fuller. *Utopia or Oblivion*. Bantam books, New York, 1970.

[3] L V Radushkevich and V M Lukyanovich. O strukture ugleroda, obrazujucegosja pri termiceskom razlozenii okisi ugleroda na zeleznom kontakte. *Zurn Fisic Chim*, 26:8895, 1952.

[4] S Ijima. Helical microtubules of graphitic carbon. *Nature*, 354:56, 1991.

[5] D S Bethune, H Kiang, M S Devries, G Gorman, and R Savoy and. J Vazquez. Cobaltcatalyzed growth of carbon nanotubes with single atomic layer walls. *Nature*, 363:605, 1993.

[6] T. Ichihashi S. Iijima. Single-shell carbon nanotubes of 1-nm diameter. *Nature*, 363:603, 1993.

[7] M M J Treacy, T W Ebbesen, and T M Gibson. Exceptionally high young's modulus observed for individual nanotubes. *Nature*, 381:678, 1996.

[8] E W Wong, P E Sheehan, and C M Lieber. Nanobeam mechanics: Elasticity, strength, and toughness of nanorods and nanotubes. *Science*, 277:1971, 1997.

[9] E Dujardin, T W Webbesen, A Krishan, P N Yianilos, and M M J Trecy. young's modulus of single-walled nanotubes. *Phys. Rev. B*, 58:14013, 1998.

[10] M R Falvo, G J Clary, R M Taylor, V Chi, F .P Brooks, and S Washburn. Bending and buckling of carbon nanotubes under large strain. *Nature*, 389:582, 1997.

[11] C Bower, R Rosen, L Jin, J Han, and O Zhou. Deformation of carbon nanotubes in nanotubepolymer composites. *Applied Physics Letters*, 74:3317, 1999.

[12] S Iijima, C Brabec, A Maiti, and J Bernholc. Structural flexibility of carbon nanotubes. *Journal of Chemical Physics*, 104:2089, 1996.

[13] C Dekker. Carbon nanotubes as molecular quantum wires. *Physics Today*, 52:22, 1999.

[14] E T Thostenson and T Chou. On the elastic properties of carbon nanotube-based composites: Modeling and characterization. *Journal of Physics D: Applied Physics*, 36:573, 2003.

[15] Y Guo and W Guo. Mechanical and electrostatic properties of carbon nanotubes under tensile loading and electric field. *Journal of Physics D: Applied Physics*, 36:805, 2003.

[16] H W Zhu, C L Xu, D H Wu, B Q Wei, R Vajtai, and P M Ajayan. Direct synthesis long single-wall carbon nanotube strands. *Science*, 296:84, 2002.

[17] R Saito, M Fujita, G Dresselhaus, and M S Dresselhaus. Electronic structure of chiral graphene tubules. *Applied Physics Letters*, 60:2204, 1992.

[18] G M Zhao. *New Research on Superconductivity*. Nova Science Publishers, Inc., New York, 2007.

[19] M S Dresselhaus, G Dresselhaus, and P Avouris. *Carbon nanotubes: synthesis, structure, properties and applications*. Springer Verlag, first edition, 2001.

[20] M M J Treacy, T W Ebbensen, and J M Gibson. Exceptionally high youngs modulus observed for individual carbon nanotubes. *Nature*, 381:678, 1996.

[21] A Krishnan, E Dujardin, T W Ebbesen, P N Yianilos, and M M J Treacy. Young's modulus of single-walled nanotubes. *Physical Review B (Condensed Matter and Materials Physics)*, 58(20):14013–14019, Nov 1998.

[22] D A McQuarrie. *Statistical Mechanics*. Harper and Row, 1976.

[23] L X Benedict, S G Louie, and M L Cohen. Heat capacity of carbon nanotubes. *Solid State Commun*, 100:177, 1996.

[24] A De Martino and R Egger. Effective low-energy theory of superconductivity in carbon nanotube ropes. *Physical Review B (Condensed Matter and Materials Physics)*, 70:014508, 2004.

[25] J Gonzalez. Superconductivity in carbon nanotube ropes. *Physical Review B (Condensed Matter and Materials Physics)*, 67:014528, 2003.

[26] Sédéki A., Caron L G, and Bourbonnais C. Superconductivity in armchair carbon nanotubes. *Physical Review B (Condensed Matter and Materials Physics)*, 65(14):140515, Apr 2002.

[27] M. Ferrier, A. Yu. Kasumov, V. Agache, L. Buchaillot, A M Bonnot, C. Naud, V. Bouchiat, R. Deblock, M. Kociak, M. Kobylko, S. Guéron, , and H. Bouchiat. Alteration of superconductivity and radial breathing modes in suspended ropes of carbon nanotubes by organic polymer coatings. *Physical Review B (Condensed Matter and Materials Physics)*, 74:241402, 2006.

[28] P Poncharal. Electrostatic deflections and electromechanical resonances of carbon nanotubes. *Science*, 283:15, 1999.

[29] D Kahn and J P Lu. Vibrational modes of carbon nanotubes and nanoropes. *Phys Rev B*, 60(9):6535, 1999.

[30] A M Rao, E Richter, S Bandow, B Chase, P C Eklund, K A Williams, S Fang, K R Subbaswamy, M Menon, A Thess, R E Smalley, G Dresselhaus, and M S Dresselhaus. Vibrational modes of carbon nanotubes and nanoropes. *Science*, 275:187, 1997.

[31] Y Q Zhang, G R Liu, and X Y Xie. Free transverse vibrations of double-walled carbon nanotubes using a theory of nonlocal elasticity. *Physical Review B (Condensed Matter and Materials Physics)*, 71:195404, 2005.

[32] Y Q Zhang, G R Liu, and X Y Xie2. Free transverse vibrations of double-walled carbon nanotubes using a theory of nonlocal elasticity. *Physical Review B (Condensed Matter and Materials Physics)*, 71:195404, 2005.

[33] K Jensen, C Girit, W Mickelson, and A Zettl. Tunable nanoresonators constructed from telescoping nanotubes. *Physical Review Letters*, 96:215503, 2006.

[34] S P Timoshenko. On the correction for shear of the differential equation for transverse vibrations of prismatic bars. *Phil. Mag.*, 41:744, 1921.

[35] J Yoon, C Q Ru, and A. Mioduchowski. Terahertz vibration of short carbon nanotubes modeled as timoshenko beams. *Transactions of the ASME*, 72:10, 2005.

[36] C E Bottani, A Li Bassi, M G Beghi, A Podesta'and P Milani, A Zakhidov, R Baughman, D A Walters, and R E Smalley. Dynamic light scattering from acoustic modes in single-walled carbon nanotubes. *Physical Review B (Condensed Matter and Materials Physics)*, 67:155407, 2003.

[37] A E H Love. *A Treatise on the Mathematical Theory of Elasticity.* Dover Publications, 1944.

[38] J C Phillips, R Braun, W Wang, J Gumbart, E Tajkhorshid, E Villa, C Chipot, R D Skeel, L Kale, and Klaus Schulten. Scalable molecular dynamics with namd. *Journal of Computational Chemistry*, 26:1781, 2005.

[39] E Lindahl, B Hess, and D Van der Spoel. Gromacs 3.0: A package for molecular simulation and trajectory analysis. *J. Mol. Modeling*, 7:306–317, 2001.

[40] D W Brenner, O A Shenderova1, J A Harrison, S J Stuart, B Ni, and S B Sinnott. A second-generation reactive empirical bond order (rebo)

potential energy expression for hydrocarbons. *Journal of Physics-Condensed Matter*, 14(4):783–802, 2002.

[41] K. Kadau, T C Germann, and P S Lomdahl. Large-scale molecular dynamics simulation of 19 billion particles. *International Journal of Modern Physics C*, 15:193, 2004.

[42] G Gao, T Cagin, and W A Goddard III. Energetics, structure, mechanical and vibrational properties of single-walled carbon nanotubes. *Nanotechnology*, 9:184, 1998.

[43] D Kahn and J P Lu. Vibrational modes of carbon nanotubes and nanoropes. *Physical Review B (Condensed Matter and Materials Physics)*, 60(9):6535–6540, Sep 1999.

[44] D W Noid, K Fukui, B G Sumpter, C Yang, and R Tuzun. Time averaged normal coordinate analysis of polymer particles. *Chem. Phys. Lett*, 316:285, 2000.

[45] G Guanghua, T Cagin, and A W Goddard III. Energetics, structure, mechanical and vibrational properties of single-walled carbon nanotubes. 1997.

[46] Ebbesen and Ajayan Endo. Large-scale synthesis of carbon nanotubes. *Nature*, 358:220–222, 1992.

[47] M Endo. Grow carbon fibers in the vapor phase. *Chem. Tech.*, 18:568, 1988.

[48] R Smalley. Growth mechanism of oriented long single walled carbon nanotubes using fast-heating chemical vapor deposition process. *Nano Letters*, 4(2):1025, 2004.

[49] M Joseyacaman, M Mikiyoshida, L Rendon, and J G Santiesteban. Catalytic growth of carbon microtubules with fullerene structure. *Applied Physics Letters*, 62(6):657, 1993.

[50] A Fonseca, K Hernadi, J B Nagy, D Bernaerts, and A A Lucas. Optimization of catalytic production and purification of buckytubes. *Journal of Molecular Catalysis a-Chemical*, 107(1), 1996.

[51] W Z Li, S S Xie, L X Qian, B H Chang, B S Zou, W Y Zhou, R Zhao, and G Wang. Large-scale synthesis of aligned carbon nanotubes. *Science*, 274(5293):1701, 1996.

[52] J Kong, H T Soh, A M Cassell, C F Quate, and H J Dai. Synthesis of individual single-walled carbon nanotubes on patterned silicon wafers. *Nature*, 395(6705):878, 1998.

[53] K Hernadi, A Fonseca, J B Nagy, D Bernaerts, A Fudala, and A A Lucas. Catalytic synthesis of carbon nanotubes using zeolite support. *Zeolites*, 17(5), 1996.

[54] L C Qin, D Zhou, A R Krauss, and D M Gruen. Growing carbon nanotubes by microwave plasma-enhanced chemical vapor deposition. *Applied Physics Letters*, 72(26):3437, 1998.

[55] T Kyotani, L F Tsai, and A Tomita. Formation of ultrafine carbon tubes by using an anodic aluminum-oxide film as a template. *Chemistry of Materials*, 7(8):1427, 1995.

[56] B Yakobsond and R Smalley. Fullerene nanotubes c1000000 and beyond. American Scientist, 1997.

[57] L X Zheng, M J O'Conell, S K Doorn, X Z Liao, Y H Zhao, E A Akhadov, M A Hoffbauer, B J Roop, Q X Jia, R C Dye, D E Peter-

son, S M Huang, J Liu, and Y T Zhu. Ultralong single-wall carbon nanotubes. *Nature Materials*, 3:673, 2004.

[58] X Liu, T Pichler, M Knupfer, M S Golden, J Fink, D A Walters, M J Casavent, J Schmidt, and R E Smalley. An electron energy-loss study of the structural and electronic properties of magnetically aligned single-walled carbon nanotubes. *Synth. Met.*, 121:1183–1186, 2001.

[59] Zhenhui Kang. Obtaining carbon nanotubes from grass. *Nanotechnology*, 16:1192–1195, 2005.

[60] J Zhao, A Martinez-Limial, and P B Balbuena. Understanding catalysed growth of single-wall carbon nanotubes. *Nanotechnology*, 16:S575–S581, 2005.

[61] D W Brenner. A second-generation reactive empirical bond order (rebo) potential energy expression for hydrocarbons. *J. Phys.: Condens. Matter*, 14:783, 2002.

[62] V N Popov, V E Van Doren, and M Balkanski. Elastic properties of single-walled carbon nanotubes. *Physical Review B*, 61(4):3078, 2000.

[63] R S Ruoff, D Quian, and W K Liu. Mechanical properties of carbon nanotubes: theoretical predictions and experimental measurements. *Physique*, 4:993–1008, 2003.

[64] E W Wong, P E Sheehan, and C M Lieber. Nanobeam mechanics: Elasticity, strength, and toughness of nanorods and nanotubes. *Science*, 277:1971, 1997.

[65] M B Nardelli, B I Yakobson, and J Bernholc. Mechanism of strain release in carbon nanotubes. *Physical Review B (Condensed Matter and Materials Physics)*, 57:R4277, 1998.

[66] C Q Ru. Effective bending stiffness of carbon nanotubes. *Physical Review B (Condensed Matter and Materials Physics)*, 62:9973, 2000.

[67] K Sohlberg, B G Sumpter, R E Tuzun, and D W Noid. Continuum methods of mechanics as a simplied approach to structural engineering of nanostructures. *Nanotechnology*, 9:30–36, 1998.

[68] G M Odegard, T S Gates, L M Nicholson, and K E Wise. Equivalent continuum modeling of nano-structured materials. Technical Report NASA/TM-2001-210863, NASA, 2001.

[69] T Vodenitcharova and L C Zhang. Equivalent continuum modeling of nano-structured materials. *Physical Review B (Condensed Matter and Materials Physics)*, 68:165401, 2003.

[70] M Arroyo and T Belytschko. Finite element methods for the non-linear mechanics of crystalline sheets and nanotubes. *Int. J. Numer. Eng*, 59:419, 2004.

[71] M Arroyo and T Belytschko. Finite crystal elasticity of carbon nanotubes based on the exponential cauchy-born rule. *Physical Review B (Condensed Matter and Materials Physics)*, 69:115415, 2004.

[72] A Krishnan, E Dujardin, T W Ebbesen, P N Yianilos, and M M J Treacy. Young's modulus of single-walled nanotubes. *Physical Review B (Condensed Matter and Materials Physics)*, 58:14013, 1998.

[73] L Chunyu and C Tsu-Wei. A structural mechanics approach for the analysis of carbon nanotubes. *International Journal of Solids and Structures*, 40(10):2487, 2003.

[74] W Jr Weaver and J M Gere. *Matrix Analysis of Framed Structures*. Van Nostrand Reinhold, fourth edition, 1990.

[75] W Weaver, S P Jr Timoshenko, and D H Young. *Vibration Problems in Engineering*. Wiley, N.Y., 1990.

[76] B Geist and J R McLaughlin. Double eigenvalues for the uniform timoshenko beam. *Appl. Math. Lett.*, 10(3):129, 1997.

[77] C D Spataru, S Ismail-Beigi, L X Bene dict, and S G Loulie. Excitonic effects and optical spectra of single-walled carbon nanotubes. *Physical Review B (Condensed Matter and Materials Physics)*, 92(7):077402, 2004.

[78] J Tersoff. New empirical model for the structural properties of silicon. *Physical Review Letters*, 56:632, 1986.

[79] J Han, A Globus, R Jaffe, and G Deardorff. Molecular dynamics simulations of carbon nanotube-based gears. *Nanotechnology*, 8:95, 1997.

[80] H S Choi, K H Kim, K H Hong, J Kim, H S Lee, J K Shin, A V Vasenkov, A I Fedoseyev, and V Kolobov. Multi-scale modeling of processing of carbon nanotubes. *Technical Proceedings of the 2005 NSTI Nanotechnology Conference and Trade Show*, 2:185, 2001.

[81] X Gong, J Liu, S Baskaran, R D Voise, and J S Young. Surfactant-assisted processing of carbon nanotube/polymer composites. *Chem. Mater.*, 12:1049, 2000.

[82] X Zhang, T Liu, T V Sreekumar, S Kumar, V C Moore, R H Hauge, and R. E. Smalley. Poly(vinyl alcohol)/swnt composite film. *Nano Lett.*, 3:1285, 2003.

[83] M Cadek, J N Coleman, V Barron, K Hedicke, and W Blau. Morphological and mechanical properties of carbon-nanotube-reinforced semicrystalline and amorphous polymer composites. *J. Appl. Phys. Lett.*, 81:5123, 2002.

[84] T Kimura, H Ago, M Tobita, S Ohshima, M Kyotani, and M Yumura. Polymer composites of carbon nanotubes aligned by a magnetic field. *Adv. Mater.*, 14:1380, 2002.

[85] R Sen, B Zhao, D Perea, M E Itkis, H Hu, J Love, E Bekyarova, and R C Haddon. Preparation of single-walled carbon nanotube reinforced polystyrene and polyurethane nanofibers and membranes by electrospinning. *Nano Lett.*, 4:459, 2004.

[86] C A Cooper, S R Cohen, A H Barber, and H D Wagner. Detachment of nanotubes from a polymer matrix. *Appl. Phys. Lett.*, 81:3873, 2002.

[87] A H Barber, S R Cohen, and H D Wagner. Static and dynamic wetting measurements of single carbon nanotubes. *Phys. Rev. Lett.*, 92(18):186103, 2004.

[88] Z Jia, Z Wang, C Xu, J Liang, B Wei, D Wu, and S Zhu. Study on poly(methyl methacrylate)/carbon nanotube composites. *Mater. Sci. Eng. A*, 271:395, 1999.

[89] AH Barber, SR Cohen, A Eitan, LS Schadler, and HD Wagner. Fracture transitions at a carbon-nanotube/polymer interface. *Advanced Materials*, 18(1):83, 2006.

[90] W Wang, P Ciselli, E Kuznetsov, T Peijs, and A H Barber. Effective reinforcement in carbon nanotube-polymer composites. *Philos Transact A Math Phys Eng Sci.*, 336(1870):1613, 2008.

[91] D J Palmer. Carbon nanotubes: sort it out! *Nano Today*, 1(4):9, 2006.

[92] T H Maiman. Stimulated optical radiation in ruby. *Nature*, 187:493, 1960.

[93] H Dai, A Javey, E Pop, D Mann, and Y Lu. Electrical transport properties and field-effect transistors of carbon nanotubes. *NANO: Brief Reports and Reviews*, 1:14, 2006.

[94] J Y Kim, M Kim, H Kim, J Joo, and J H Choi. Electrical and optical studies of organic light emitting devices using swcnts-polymer nanocomposites. *Optical Materials*, 21:147, 2002.

[95] J H Chen, Z P Huang, D Z Wang, S X Yang, W Z Li, , J G Wen, and Z F Ren. Electrochemical synthesis of polypyrrole films over each of well-aligned carbon nanotubes. *Synth. Met*, 125:289, 2002.

[96] M Hughes, M S P Shaffer, A C Renouf, C Singh, G Z Chen, D J Fray, and A H Windle. Electrochemical capacitance of nanocomposite films formed by coating aligned arrays of carbon nanotubes with polypyrrole. *Adv. Mat.*, 14:382, 2002.

[97] L Dai. Light-emmiting polymers and carbon nanotube electron emitters for optoelectronic displays. *Smart Mater. Struct.*, 11:645, 2002.

[98] J M Li. Fabrication of a carbon nanotube drive shaft component. *Nanotechnology*, 15:551, 2004.

[99] S J Tans, A R M Verschueren, and C Dekker. Room-temperature transistor based on a single carbon nanotube. *Nature*, 393:49, 1998.

[100] J B Cui, M Burghard, and K Kern. Room temperature single electron transistor by local chemical modification of carbon nanotubes. *Nano Letters*, 2:117, 2002.

[101] S Heinze, J Tersoff, and P Avouris. Electrostatic engineering of nanotube transistors for improved performance. *Appl. Phys. Lett.*, 83:5038, 2003.

[102] S I Lee, S W Howell, A Raman, R Reifenberger, C V Nguyen, and M Meyyappan. Nonlinear tapping dynamics of multi-walled carbon nanotube tipped atomic force microcantilevers. *Nanotechnology*, 15:416, 2004.

[103] C Li and T-W Chou. Vibrational behaviors of multiwalled-carbon-nanotube-based nanomechanical resonators. *Appl. Phys. Lett.*, 84:121, 2004.

[104] A G Lipson, B F Lyakhov, E I Saunin, and A Y Tsivadze. Evidence for large hydrogen storage capacity in single-walled carbon nanotubes encapsulated by electroplating pd onto a pd substrate. *Phys. Rev. B*, 77:081405, 2008.

[105] H Maruyama, S H Yoshimura, and S Akita. Covalent attachment of protein to the tip of a multiwalled carbon nanotube without sidewall decoration. *J. Appl. Phys*, 102:094701, 2007.

[106] B J Hinds, N Chopra, T Rantell, R Andrews, and V Gavalas L G Bachas. Aligned multiwalled carbon nanotube membranes. *Science*, 303:62, 2004.

[107] H M Kim, K Kim, C Y Lee, J Joo, S J Cho, H S Yoon, D A Pejakovic, J W Yoo, and A Epstein. Electrical conductivity and electromagnetic interference shielding of multiwalled carbon nanotube composites containing fe catalyst. *J. Appl. Phys. Lett.*, 84:589, 2004.

[108] J D Isaacs, A C Vine, H Bradner, and G E Bachus. Satellite elongation into a true sky-hook. *Science*, 151:682, 1966.

[109] W T Thomson. *Theory of vibration with Applications*. Nelson Thornes, fourth edition, 1993.

[110] W Weaver, S P Jr Timoshenko, and D H Young. *Vibration Problems in Engineering*. Wiley, New York, 1990.

[111] L H Donell. A discussion of thin shell theory. In New York Jon Willey, editor, *Proc. 5th Int. Congress of Applied Mechanics*, pages 66–70, 1938.

[112] Kh M Mushtari. Certain generalizations of the theory of thin shells. *Izv. Fiz. Mat. Kaz.*, 11(8), 1938.

[113] S Markus. *The Mechanics of Vibrations of Cylindrical Shells*. Elsevier, Amsterdam, 1988.

[114] W Soedel. A new frequency formula for closed circular cylindrical shells for a large variety of boundary conditions. journal of sound and vibration. *Journal of Sound Vibration*, 70(3):309–317, 1980.

[115] J L Sewall and E C Naumann. Vibration tests and analysis of thin cylindrical shells with and without longitudinal stiffeners. *NASA TN D-4705*, 1968.

[116] W D Cornell, P Cieplak, C I Bayly, I R Gould, Jr. K M Merz, D M Ferguson, D C Spellmeyer, T Fox, J W Caldwell, and P A Kollman. A second generation force field for the simulation of proteins, nucleic acids, and organic molecules. *J. Am. Chem. Soc.*, 117:5179–5197, 1995.

[117] C Li and T W Chou. Elastic properties of single-walled carbon nanotubes in transverse directions. *Int. J. Solids Struct.*, 40:2487, 2003.

[118] M Levinson and D W Cooke. On the two frequency spectra of timoshenko beams. *Journal of Sound and Vibration*, 84(3):319–326, 1982.

[119] E Buckingham. On physically similar systems; illustrations of the use of dimensional equations. *Physical Review*, 4(4):345–376, Oct 1914.

[120] D W Noid, K Fukui, B G Sumpter, C Yang, and R Tuzun. Time averaged normal coordinate analysis of polymer particles. *Chem. Phys. Lett.*, 316:285, 2000.

[121] J T Frey and D J Doren. Tubegen 3.3f. University of Delaware, Newark DE, 2004.

[122] R H Byrd, P Lu, and J Nocedal. A limited memory algorithm for bound constrained optimization. *SIAM Journal on Scientific and Statistical Computing*, 16(5):1190–1208, 1995.

[123] H J C Berendensen, J P M Postma, W F van Gunsteren, A DiNola, and J R Haak. Molecular dynamics with coupling to an external bath. *J.Chem. Phys.*, 81:3684, 1984.

[124] Python. Copyright ©1990-2006, Python Software Foundation.

[125] VPhython. Copyright ©2000 by David Scherer.

[126] J W Mintmire and C T White. Electronic and structural properties of carbon nanotubes. *Carbon*, 33(7):893, 1995.

[127] D J Ewins. *Modal Testing: Theory, Practice and Applications*. Taylor & Francis Group, second edition, 2001.

[128] W Soedel. *Vibrations of Shells and Plates*. Marcel Dekker, Inc., New York, third edition, 2004.

[129] Y Huang, J wu, and K C Hwang. Thickness of graphene and single-wall carbon nanotubes. *Physical Review B (Condensed Matter and Materials Physics)*, 74:245413, 2006.

[130] C L Dym and I H Shames. *Solid mechanics: a variational approach*. Mc Graw Hill, 1973.

[131] L Meirovitch. *The Mechanics of Vibrations of Cylindrical Shells*. Elsevier, Amsterdam, 1988.

[132] J Hone, M C Llaguno, M J Biercuk, A T Johnson, B Batlogg, Z Benes, and J E Fischer. Thermal properties of carbon nanotubes and nanotube-based materials. *Applied Physics A: Materials Science and Processing*, 74:339–343, 2004.

[133] Chunyu Li and Tsu-Wei Chou. Quantized molecular structural mechanics modeling for studying the specific heat of single-walled carbon nanotubes. *Physical Review B (Condensed Matter and Materials Physics)*, 71(7):075409, 2005.

[134] M W Zemansky and R H Dittman. *Heat and thermodynamics : an intermediate textbook*. New York : McGraw-Hill, seventh edition, 1997.

[135] L X Benedict, S G Louie, and M L Cohen. Heat capacity of carbon nanotubes. *Solid State Communications*, 100(177), 1996.

[136] W. Yi, L. Lu, Zhang Dian-lin, Z. W. Pan, and S. S. Xie. Linear specific heat of carbon nanotubes. *Physical Review B (Condensed Matter and Materials Physics)*, 59(14):R9015–R9018, 1999.

[137] Ari Mizel, Lorin X. Benedict, Marvin L. Cohen, Steven G. Louie, A. Zettl, Nasser K. Budraa, and W. P. Beyermann. Analysis of the low-temperature specific heat of multiwalled carbon nanotubes and carbon nanotube ropes. *Physical Review B (Condensed Matter and Materials Physics)*, 60(5):3264–3270, Aug 1999.

[138] L B Biedermann, R C Tung, A Raman, and R G Reifenberger. Flexural vibration spectra of carbon nanotubes measured using laser doppler vibrometry. *Nanotechnology*, 20:35702, 2009.

Appendix A

Visualization of a selected group of normal modes

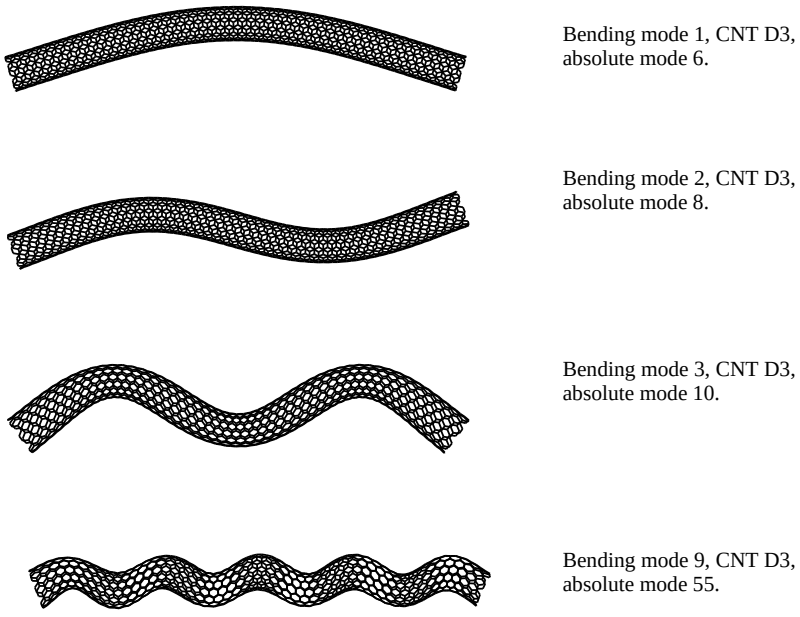

Figure A.1: A sample of bending modes for CNT D3.

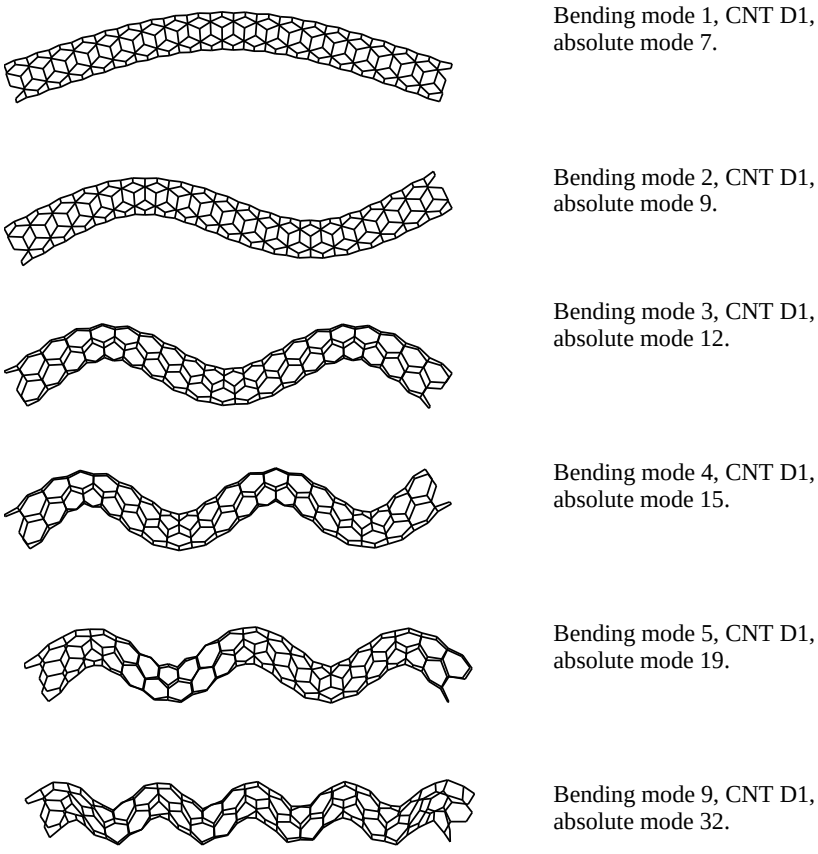

Figure A.2: A sample of bending modes for CNT D1.

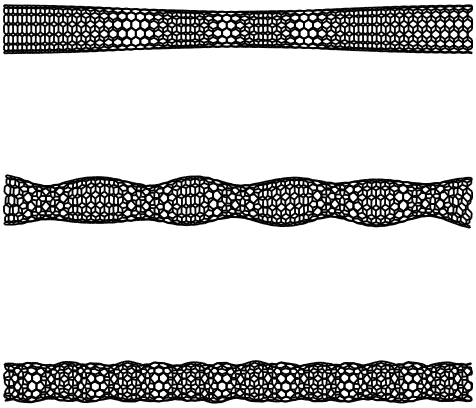

Figure A.3: A sample of twisting modes, CNT D3.

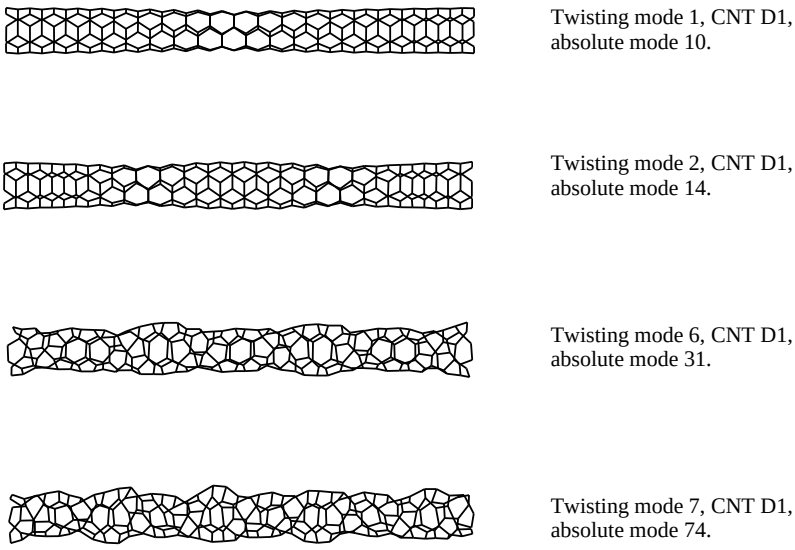

Figure A.4: A sample of twisting modes, CNT D1.

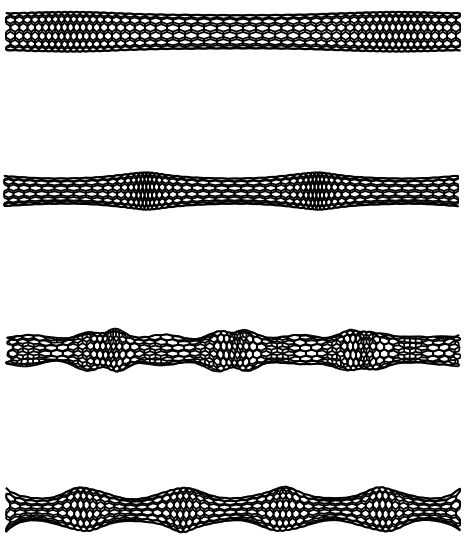

Figure A.5: A sample of stretching modes, CNT D3.

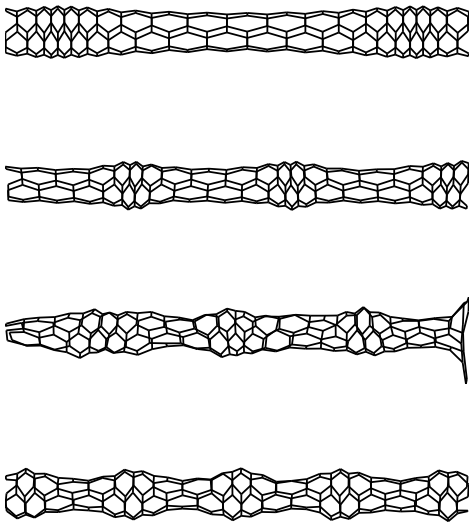

Figure A.6: A sample of stretching modes, CNT D1.

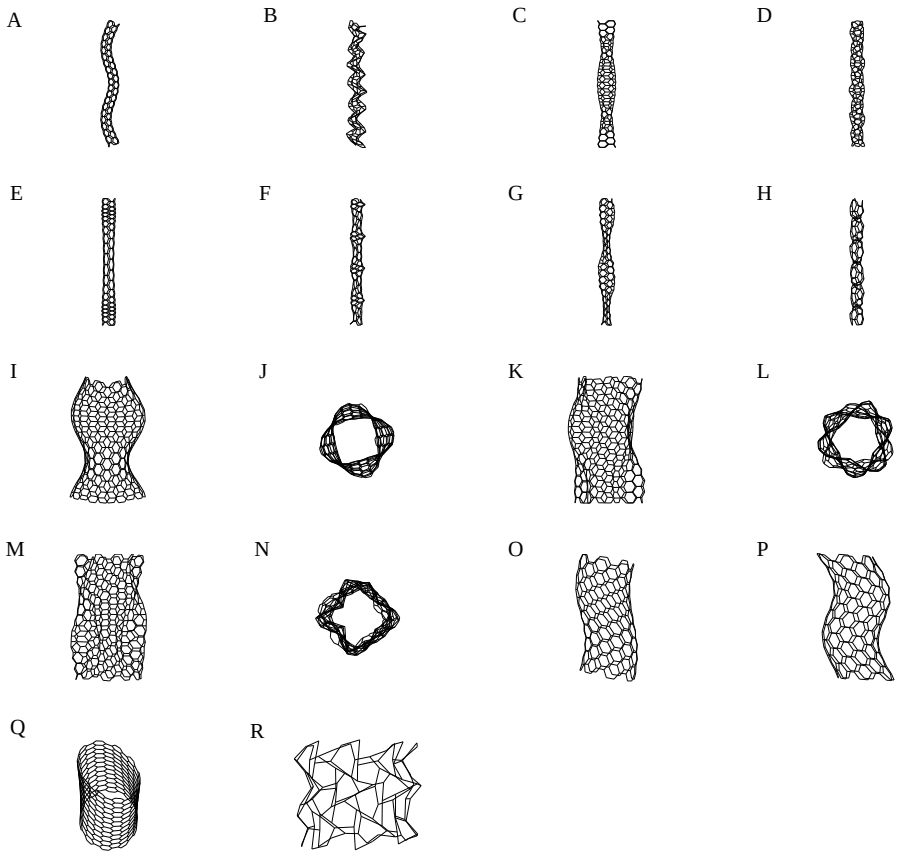

Figure A.7: A: Third bending mode of nanotube D1, B: Thirteen bending number of nanotube D1, C: Second twisting mode of nanotube D1, D: Seventh twisting mode of nanotube D1, E: Third stretching mode of nanotube D1, F: Eighth stretching mode of nanotube D1, G: Third breathing mode of nanotube D1, H: Seventh breathing mode of nanotube D1, I: Side view of shell mode n=2, m=3, nanotube C4, J: Top view of shell mode n=2, m=3, nanotube C4, K: Side view of shell mode n=3, m=2, nanotube C4, L: Top view of shell mode n=3, m=2, nanotube C4, M: Side view of shell mode n=4, m=1, nanotube C4, N: Top view of shell mode n=4, m=1, nanotube C4, O: Bending mode 2, nanotube C3, P: Another bending mode 2, nanotube C3, Q: New visualised mode, nanotube C3, R: Fourth bending mode of nanotube B3

Appendix B

Python-programmed codes and adjustments to GROMACS parameter files

All Python-proggramed codes are included in a CD-ROM included in this thesis.

B.1 Energy minimization parameter file - em.mdp

```
cpp                =  /lib/cpp
define             =  -DFLEX_SPC
constraints        =  none
integrator              = l-bfgs
nsteps             =  300000
nstlist            =  0
pbc                =  no
emtol              =  0.0000001
```

```
emstep              =  0.01
epsilon_r           = 0.000001
nstcomm             =  - 1
ns_type             =  simple
rlist               =  0.0
rcoulomb            =  0.0
rvdw                =  0.0
coulombtype         =  cut-off
Tcoupl              =  no
Pcoupl              =  no
gen_vel             =  no
```

B.2 Molecular dynamics parameter file - md.mdp

```
cpp                 = /lib/cpp
include             = -I../top
define              =
integrator          = md
dt                  = 0.001
nsteps              = 100000
nstxout             = 200
nstvout             = 200
nstlog              = 200
nstenergy           = 200
nstxtcout           = 200
nstlist             = 200
pbc                 = no
nstcomm             = -1
ns_type             = Simple
rlist               = 0.0
rcoulomb            = 0.0
rvdw                = 0.0
coulombtype         = cut-off
Tcoupl              = berendsen
tc-grps             = System
tau-t               = 0.1
ref_t               = 0.1
Pcoupl              = no
gen_vel             = no
```

B.3 Normal mode analysis parameter file - nm.mdp

```
cpp                      = /lib/cpp
include                  = -I../top
integrator               = nm
pbc                =  no
nstcomm            =  -1
ns_type            =  simple
rlist              =  0.0
rcoulomb           =  0.0
rvdw               =  0.0
coulombtype        =  cut-off
Tcoupl             =  no
Pcoupl             =  no
gen_vel            =  no
```